Supplementary Information for the paper
The efficiency of synchronization dynamics and the role of network syncreactivity

Supplementary Note 1. GENERAL COUPLING FUNCTION

In this section, we discuss the case of having a general nonlinear coupling function $\boldsymbol{H}(\boldsymbol{x})$. The equations that describe the network dynamics are

$$\dot{\boldsymbol{x}}_i(t) = \boldsymbol{F}(\boldsymbol{x}_i(t)) + \sigma \sum_{j=1}^{N} L_{ij} \boldsymbol{H}(\boldsymbol{x}_j(t)), \quad i = 1, \dots, N. \tag{S1}$$

The steps to retrieve the equation of the dynamics of the transverse perturbations are similar to the case of having a coupling matrix H. A slight difference is that H should be replaced by $\boldsymbol{DH}(\boldsymbol{s}(t))$ in those steps where $\boldsymbol{DH}(\boldsymbol{s}(t))$ is the Jacobian of $\boldsymbol{H}$ evaluated at $\boldsymbol{s}(t)$. Therefore, the transverse perturbations dynamics are described by the following equation,

$$\begin{aligned} \delta\dot{\hat{\boldsymbol{X}}}(t) &= \left[I_{N-1} \otimes \boldsymbol{DF}(\boldsymbol{s}(t)) + \sigma L^{\perp} \otimes \boldsymbol{DH}(\boldsymbol{s}(t))\right] \delta\hat{\boldsymbol{X}} \\ &= \hat{Z}(\boldsymbol{s}(t)) \delta\hat{\boldsymbol{X}}(t). \end{aligned} \tag{S2}$$

The dynamics of the experimental system studied in Sec. IID of the main paper can also be linearized about the synchronous solution, resulting in an equation in the same form of (S2). Then, the transverse reactivity of the perturbations about $\boldsymbol{x}_s$ on the synchronous solution

$$\begin{aligned} r(\boldsymbol{x}_s) :=& \frac{1}{2} e_1 \left(\hat{Z}^{\top}(\boldsymbol{x}_s) + \hat{Z}(\boldsymbol{x}_s)\right) \\ =& \frac{1}{2} e_1 \Big(I_{N-1} \otimes [\boldsymbol{DF}(\boldsymbol{x}_s) + \boldsymbol{DF}^{\top}(\boldsymbol{x}_s)] \\ & \qquad + \sigma ({L^{\perp}}^{\top} + L^{\perp}) \otimes [\boldsymbol{DH}(\boldsymbol{x}_s) + \boldsymbol{DH}^{\top}(\boldsymbol{x}_s)] \Big). \end{aligned} \tag{S3}$$

The difference to the case of having a positive semidefinite coupling matrix H is that now the symmetric matrix in the argument of e_1 cannot be reduced in size as before.

To evaluate the transverse reactivity $r(\boldsymbol{x}_s)$, the largest eigenvalue of the matrix $(\hat{Z}^{\top}(\boldsymbol{x}_s) + \hat{Z}(\boldsymbol{x}_s))/2 \in \mathbb{R}^{m(n-1)}$ must be found. If the number of nodes n is large, the computational complexity of calculating this eigenvalue can be expensive. However, since only the largest eigenvalue is required, not the entire spectrum, one can take advantage of efficient methods to compute the largest eigenvalue of a symmetric matrix. References[1–4] provide a few examples of such methods. The rest of the results presented in the main text can then be derived, as well as the formulation of the time-varying coupling strategies, with the only difference that $r(\boldsymbol{x}_s)$ should be calculated using Eq. (S3).

Supplementary Note 2. LONG-TIME DISCRETE REACTIVITY

Consider the linear time-invariant discrete-time system $\boldsymbol{x}_{k+1} = A\boldsymbol{x}_k$. Reference[5] defined the discrete-time reactivity for this system as

$$r = \sigma_1(A) - 1, \tag{S4}$$

where $\sigma_1(A)$ denotes the largest singular value of the matrix A. Here, we aim to extend this definition for reactivity larger than one step. For a general case, we consider n step into the future.

We define the n-step ahead reactivity of a linear-time varying system $\boldsymbol{x}_{k+1} = A_k \boldsymbol{x}_k$ based on

$$\begin{aligned} r_n(k) &:= \max_{\boldsymbol{x}_k \neq 0} \left[\left(\frac{\|\boldsymbol{x}_{k+n}\| - \|\boldsymbol{x}_k\|}{\|\boldsymbol{x}_k\|} \right) \right] \\ &= \max_{\boldsymbol{x}_k \neq 0} \left[\left(\frac{\sqrt{\boldsymbol{x}_{k+n}^{\top} \boldsymbol{x}_{k+n}} - \sqrt{\boldsymbol{x}_k^{\top} \boldsymbol{x}_k}}{\sqrt{\boldsymbol{x}_k^{\top} \boldsymbol{x}_k}} \right) \right] \\ &= \max_{\boldsymbol{x}_k \neq 0} \left[\sqrt{\frac{\boldsymbol{x}_k^{\top} (\prod_{m=0}^{n-1} A_{k+m})^{\top} (\prod_{m=0}^{n-1} A_{k+m}) \boldsymbol{x}_k}{\boldsymbol{x}_k^{\top} \boldsymbol{x}_k}} \right] - 1 \\ &= \sigma_1 \left(\prod_{m=0}^{n-1} A_{k+m} \right) - 1, \end{aligned} \tag{S5}$$

where $\prod$ is the product operator. Here, the reactivity $r_n(k)$ returns the maximum growth after n steps initiated at time step k. For example, the two-step reactivity initiated at time $k = 0$ is $r_2(0) = \sigma_1(A_1 A_0) - 1$, and the 2-step ahead reactivity initiated at time $k = 5$ is $r_2(5) = \sigma_1(A_6 A_5) - 1$. It is important to differentiate the initiation time k since for the last two examples, $A_1 A_0$ might not be equal to $A_6 A_5$ in general.

A. Relation to Lyapunov exponents

Consider a discrete-time map $\boldsymbol{x}_{k+1} = \boldsymbol{M}(\boldsymbol{x}_k)$. Assume the system is initialized at $\boldsymbol{x}_0$. The time evolution of the infinitesimal perturbations $\boldsymbol{y}_k$ tangent to $\boldsymbol{x}_0$ is

$$\boldsymbol{y}_{k+1} = \boldsymbol{DM}(\boldsymbol{x}_0) \boldsymbol{y}_k. \tag{S6}$$

The n step perturbations are $\boldsymbol{y}_n = \boldsymbol{DM}^n(\boldsymbol{x}_0) \boldsymbol{y}_0$ where

$$\boldsymbol{DM}^n(\boldsymbol{x}_0) = \boldsymbol{DM}(\boldsymbol{x}_{n-1}) \boldsymbol{DM}(\boldsymbol{x}_{n-2}) \cdots \boldsymbol{DM}(\boldsymbol{x}_0).$$

The Lyapunov exponent is defined for the initial condition $\boldsymbol{x}_0$ and the initial orientation of the infinitesimal perturbations $\boldsymbol{u}_0 = \boldsymbol{y}_0/\|\boldsymbol{y}_0\|$ as (see[6] (Chapter 4.4))

$$\begin{aligned} h(\boldsymbol{x}_0, \boldsymbol{u}_0) &= \lim_{n\to\infty} \frac{1}{n} \log\left(\frac{\|\boldsymbol{y}_n\|}{\|\boldsymbol{y}_0\|}\right) \\ &= \lim_{n\to\infty} \frac{1}{n} \log \|\boldsymbol{DM}^n(\boldsymbol{x}_0)\boldsymbol{u}_0\| \\ &= \lim_{n\to\infty} \frac{1}{2n} \log \sqrt{\boldsymbol{u}_0^\top \boldsymbol{DM}^n(\boldsymbol{x}_0)^\top \boldsymbol{DM}^n(\boldsymbol{x}_0)\boldsymbol{u}_0}. \end{aligned}$$

Since the length of the vector $\boldsymbol{x}$ is N, there are N or fewer distinct Lyapunov exponents. The maximum Lyapunov exponent corresponds to the largest eigenvalue of the matrix $\boldsymbol{DM}^n(\boldsymbol{x}_0)^\top \boldsymbol{DM}^n(\boldsymbol{x}_0)$, or equivalently, the largest singular value of the matrix $\boldsymbol{DM}^n(\boldsymbol{x}_0)$. Hence,

$$MLE(\boldsymbol{x}_0) = \lim_{n\to\infty} \frac{1}{2n} \log \sigma_1(\boldsymbol{DM}^n(\boldsymbol{x}_0)). \tag{S7}$$

The long-term reactivity associated with Eq. (S6) is

$$r_n(\boldsymbol{x}_0) = \sigma_1\left(\prod_{m=0}^{n-1} \boldsymbol{DM}(\boldsymbol{x}_m)\right) - 1 = \sigma_1\left(\boldsymbol{DM}^n(\boldsymbol{x}_0)\right) - 1.$$

Hence, in the limit of $n \to \infty$,

$$MLE(\boldsymbol{x}_0) = \lim_{n\to\infty} \frac{1}{2n} \log(r_n(\boldsymbol{x}_0) + 1). \tag{S8}$$

Equation (S8) explicitly connects the maximum Lyapunov exponent to the long-term reactivity defined in (S5) in the limit of $n \to \infty$.

Supplementary Note 3. ROLE OF THE INITIAL CONDITIONS AND OF THE NETWORK TOPOLOGY

Next, we present an example to illustrate the effects of reactivity on the synchronization dynamics. Without loss of generality, we consider the case of chaotic Lorenz oscillators, coupled in the second state variable, for which,

$$\boldsymbol{x} = \begin{bmatrix} x \\ y \\ z \end{bmatrix}, \quad \boldsymbol{F}(\boldsymbol{x}) = \begin{bmatrix} 10(y-x) \\ x(28-z)-y \\ xy-2z \end{bmatrix}, \quad H = \begin{bmatrix} 0 & 0 & 0 \\ 0 & 1 & 0 \\ 0 & 0 & 0 \end{bmatrix}. \tag{S9}$$

We evaluate the transverse perturbation $\delta\bar{\boldsymbol{X}}(t)$ by simulating the full nonlinear complex system

$$\dot{\boldsymbol{x}}_i(t) = \boldsymbol{F}(\boldsymbol{x}_i(t)) + \sigma \sum_{j=1}^{N} L_{ij} H \boldsymbol{x}_j(t), \quad i = 1, \dots, N. \tag{S10}$$

Further details on how we performed this calculation can be found in Sec. Supplementary Note 3 A. In what follows, we plot the norm of the perturbations transverse to the synchronous solution for the case of I) different initial conditions with a fixed network topology and II) different network topologies with fixed initial conditions.

Case I): We first fix the network topology, which is shown in Supplementary Fig. 1 (B), and set two different initial conditions for Eq. (S10), which are chosen to be close to (but not on) the synchronous solution. The first set of 'reactive initial conditions' is close to be a point $\boldsymbol{s}(0)$ from the reactive region $\mathcal{R}$ of the attractor (shown as a red point in Supplementary Fig. 1 (B)),

$$\boldsymbol{x}_1(0) = \begin{bmatrix} -0.4037 \\ -0.7118 \\ 16.6279 \end{bmatrix}, \ \boldsymbol{x}_2(0) = \begin{bmatrix} -0.4035 \\ -0.7117 \\ 16.6276 \end{bmatrix},$$
$$\boldsymbol{x}_3(0) = \begin{bmatrix} -0.3988 \\ -0.7100 \\ 16.6213 \end{bmatrix}, \ \boldsymbol{s}(0) = \begin{bmatrix} -0.3995 \\ -0.7103 \\ 16.6222 \end{bmatrix};$$

and the second set of 'non-reactive initial conditions' is chosen to be close to a point $\boldsymbol{s}(0)$ from the nonreactive region $\mathcal{N}$ of the attractor (shown as a blue point in Supplementary Fig. 1 (B)),

$$\boldsymbol{x}_1(0) = \begin{bmatrix} -14.0976 \\ -7.4904 \\ 41.5723 \end{bmatrix}, \ \boldsymbol{x}_2(0) = \begin{bmatrix} -14.1001 \\ -7.4870 \\ 41.5713 \end{bmatrix},$$
$$\boldsymbol{x}_3(0) = \begin{bmatrix} -14.1051 \\ -7.4802 \\ 41.5695 \end{bmatrix}, \ \boldsymbol{s}(0) = \begin{bmatrix} -14.0997 \\ -7.4875 \\ 41.5715 \end{bmatrix}.$$

We set $\sigma = 10.8$ such that the synchronous solution is stable (long-term stability) based on the master stability function[7]. We simulate Eq. (S10) with the two sets of reactive and non-reactive initial conditions. Supplementary Fig. 1 (A) shows the norm of the transverse perturbations $\|\delta\bar{\boldsymbol{X}}(t)\|$ at initial times obtained from each of the two sets of initial conditions. We see a peak of $\|\delta\bar{\boldsymbol{X}}(t)\|$ at initial times for the set of reactive initial conditions and no peaks for the set of non-reactive conditions. Supplementary Fig. 1 (B) shows the reactive and non-reactive regions based on our proposed theory. We see that when the initial conditions for the oscillators are chosen close to a point on the reactive region, the norm of the transverse perturbations increases at initial times, while this norm does not increase when the initialization is in the non-reactive region. Our numerical results in Supplementary Fig. 1 illustrate how reactivity may affect the transient dynamics toward synchronization.

Case II): We set two different network topologies and fix the initial condition for Eq. (S10). The initial conditions for the reactive and non-reactive cases are the same

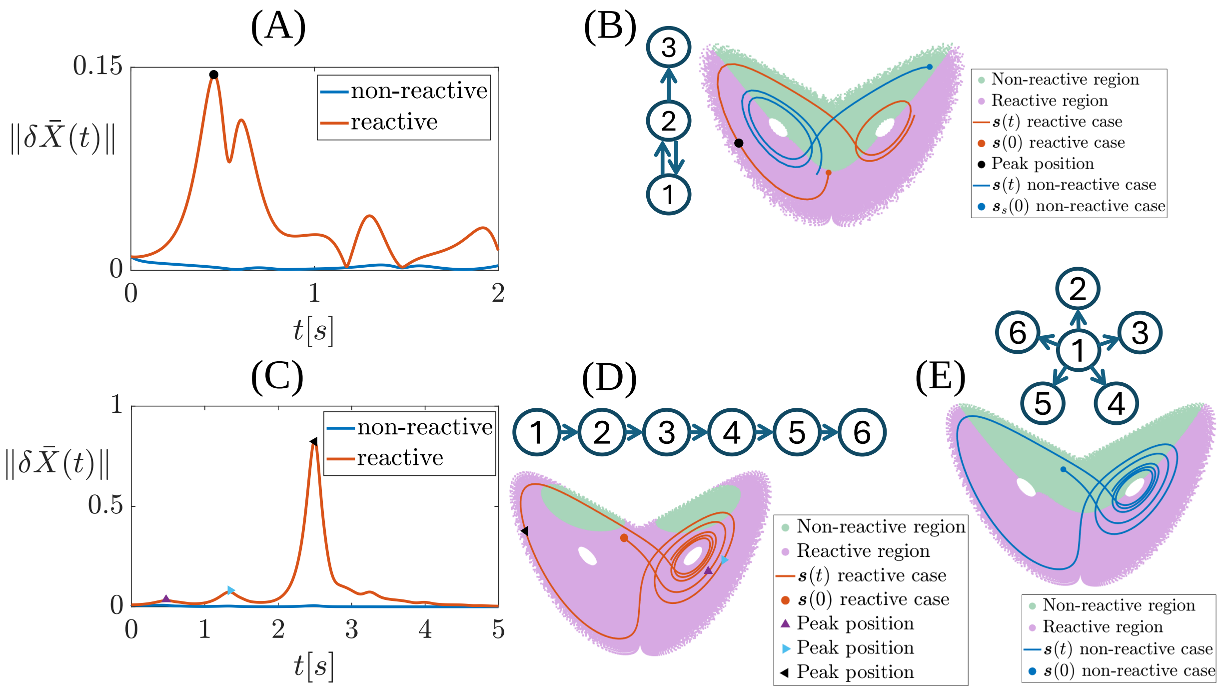

Supplementary Fig. 1. **Case I: fixed network and different initial conditions (Panels A and B).** Panel (A) shows the norm of the transverse perturbations associated with Eq. (S10) at initial times; panel (B) shows the topology of the network and the reactive (lavender color) and non-reactive (green color) regions of the Lorenz attractor for the selected σ, ξ and H. **Case II: fixed initial condition and different networks (Panels C, D, and E).** Panel (C) shows the norm of the transverse perturbations at initial times; panel (D) shows the reactive topology and the reactive (lavender color) and non-reactive (green color) regions of the Lorenz attractor; panel (E) shows the non-reactive topology and the reactive (lavender color) and non-reactive (green color) regions of the Lorenz attractor. The same set of initial conditions for Eq. (S10) is set for both the reactive and non-reactive network topologies in panels (D) and (E).

as

$$\boldsymbol{x}_1(0) = \begin{bmatrix} -2.3124 \\ 3.3403 \\ 31.2333 \end{bmatrix}, \ \boldsymbol{x}_2(0) = \begin{bmatrix} -2.3105 \\ 3.3454 \\ 31.2345 \end{bmatrix},$$

$$\boldsymbol{x}_3(0) = \begin{bmatrix} -2.3093 \\ 3.3487 \\ 31.2353 \end{bmatrix}, \ \boldsymbol{x}_4(0) = \begin{bmatrix} -2.3087 \\ 3.3505 \\ 31.2358 \end{bmatrix},$$

$$\boldsymbol{x}_5(0) = \begin{bmatrix} -2.3085 \\ 3.3509 \\ 31.2359 \end{bmatrix}, \ \boldsymbol{x}_6(0) = \begin{bmatrix} -2.3089 \\ 3.3500 \\ 31.2356 \end{bmatrix},$$

$$\boldsymbol{s}(0) = \begin{bmatrix} -2.3097 \\ 3.3476 \\ 31.2351 \end{bmatrix}.$$

The norm of the transverse deviations at $t = 0$ is $\|\delta\bar{\boldsymbol{X}}(0)\| = 0.01$. The topology in Supplementary Fig. 1(D) is a 6-node directed chain network with $\lambda_2 = -1$ and $\xi = 0.042$. The other topology shown in Supplementary Fig. 1(E) is a 6-node directed star network with $\lambda_2 = \xi = -1$. We set $\sigma = 6$ for both topologies; thus the long-term stability of the synchronous solution for both networks is the same, although their values of ξ are different. Consequently, the critical probability μ from

$$\mu = \frac{1}{2} + \frac{1}{2}\Big\langle \operatorname{sign}\Big(r(\boldsymbol{x}_s)\Big)\Big\rangle_{\mathcal{A}}, \tag{S11}$$

is also different. Namely, $\mu = 0.88$ for the chain network and $\mu = 0.57$ for the star network, which can be seen by comparing panels (D) and (E). In Supplementary Fig. 1 (C) we plot the norm of the transverse perturbations $\|\delta\bar{\boldsymbol{X}}(t)\|$ at initial times, obtained for each one of the two network topologies in (D) and (E) respectively. We see a succession of three peaks in $\|\delta\bar{\boldsymbol{X}}(t)\|$ at the initial times for the network in panel (D) and no peaks for the network in panel (E). The peaks seen in (D) always occur about the part of the attractor for which the transverse reactivity is the largest. We see that even when networks have the same synchronizability, the transient dynamics of the nonlinear system is strongly affected by the reactivity, resulting in large transient deviations from the synchronous solution for networks with larger ξ.

A. Calculation of nonlinear transverse motions

Here we clarify how we calculated the transverse perturbations for the examples in Supplementary Note 3 and

Fig. 1 of the main manuscript. First, we simulate both Eqs. (S10) and

$$\dot{\boldsymbol{s}}(t) = \boldsymbol{F}(\boldsymbol{s}(t)), \tag{S12}$$

to obtain $\boldsymbol{x}_i(t)$ and $\boldsymbol{s}(t)$, respectively. Then, the perturbations $\delta\boldsymbol{x}_i(t) = \boldsymbol{x}_i(t) - \boldsymbol{s}(t)$, $i = 1, \dots, N$, are calculated and stacked on top of each other to form $\delta\boldsymbol{X}(t) = [\delta\boldsymbol{x}_1(t)^\top, \ \delta\boldsymbol{x}_2(t)^\top, \ \cdots, \delta\boldsymbol{x}_N(t)^\top]^\top$. We calculate the perturbations transverse to the synchronous solution as $\delta\bar{\boldsymbol{X}}(t) = (V^\top \otimes I_3)\delta\boldsymbol{X}(t)$. The matrix $V \in \mathbb{R}^{N \times N-1}$ is an orthonormal basis for the null subspace of $[1\ 1 \dots 1] \in \mathbb{R}^{1 \times N}$ Finally, the norm of the transverse motion $\|\delta\bar{\boldsymbol{X}}(t)\|$ is plotted in Supplementary Fig. 1 and Fig. 1 of the main manuscript.

We note that the vector $\delta\bar{\boldsymbol{X}}(t)$ and the vector $\delta\hat{\boldsymbol{X}}(t)$ from

$$\delta\dot{\hat{\boldsymbol{X}}}(t) = [I_{n-1} \otimes \boldsymbol{DF}(\boldsymbol{s}(t)) + \sigma L^\perp \otimes H]\delta\hat{\boldsymbol{X}} = \hat{Z}(\boldsymbol{s}(t))\delta\hat{\boldsymbol{X}}(t), \tag{S13}$$

are similar in the sense that they both represent the transverse motion, but their evaluation is different since $\delta\bar{\boldsymbol{X}}(t)$ is calculated by simulating the nonlinear coupled system in Eq. (S10), while $\delta\hat{\boldsymbol{X}}(t)$ is calculated through Eq. (S13) which is the linearized dynamics about the synchronous solution. We thus expect $\delta\hat{\boldsymbol{X}}(t)$ to be equal to $\delta\bar{\boldsymbol{X}}(t)$ as long as the perturbations are small.

Supplementary Note 4. BOUNDS OF ALGEBRAIC CONNECTIVITY ξ

Here, we provide a lower and upper bound for the algebraic connectivity ξ, by using the Cauchy interlacing theorem.

Proposition 1. *The algebraic connectivity ξ of the Laplacian L is bounded by the largest and the second largest eigenvalues of the symmetric part of L, i.e., $S = (L + L^\top)/2$.*

Proof. We remove a row and column from the transformed Laplacian $\tilde{L} = V^\top L V$ to retrieve the reduced size Laplacian $L^\perp$. Then, we calculate the symmetric part of $\tilde{L}$, $\tilde{S} = (\tilde{L} + \tilde{L}^\top)/2$ and the symmetric part of $L^\perp$, $\hat{S} = (L^\perp + {L^\perp}^\top)/2$. The matrix $\hat{S}$ is now a principle submatrix of $\tilde{S}$. Hence, based on the Cauchy interlacing theorem, the eigenvalues of $\hat{S}$ are interlaced within those of $\tilde{S}$. Since V is a similarity transformation and preserves the eigenvalues, the eigenvalues of $\tilde{S}$ and S coincide. Therefore, ξ is upper bounded by the largest and lower bounded by the second largest eigenvalues of S. □

Corollary 1. *The algebraic connectivity ξ of the 'minimally reactive networks'[8] with the Laplacian matrix L are non-positive.*

Proof. For minimally reactive networks, the reactivity of the Laplacian matrix L is zero, i.e., the largest eigenvalue of $S = (L + L^\top)/2$ is zero (Theorem 1 in Ref.[8]). Therefore, the algebraic connectivity $\xi \leq 0$. □

Supplementary Note 5. REACTIVITY OF DIFFERENT ATTRACTORS

In this section, we plot the reactivity $r(\boldsymbol{x}_s)$ for points on the attractor, $\boldsymbol{x}_s \in \mathcal{A}$, for selected chaotic systems. The chaotic systems are Lorenz, Rossler, Chen, Forced Van Der Pol, the FitzHugh-Nagumo model, and the Hindmarsh–Rose model. We simulated each system for a long time (5000 s) and evaluated the reactivity $r(\boldsymbol{x}_s)$ using

$$r(\boldsymbol{x}_s) = e_1\left(\frac{\boldsymbol{DF}(\boldsymbol{x}_s) + \boldsymbol{DF}^\top(\boldsymbol{x}_s)}{2} + \sigma\xi H\right). \tag{S14}$$

For all cases, we set $\sigma\xi = -1$. For Forced Van Der Pol and the FitzHugh-Nagumo model, we used

$$H = \begin{bmatrix} 0 & 0 \\ 0 & 1 \end{bmatrix}, \tag{S15}$$

and for the rest of the systems, we set

$$H = \begin{bmatrix} 1 & 0 & 0 \\ 0 & 0 & 0 \\ 0 & 0 & 0 \end{bmatrix}. \tag{S16}$$

Supplementary Fig. 2 shows the reactivity $r(\boldsymbol{x}_s)$ over the attractor of the selected chaotic systems. We see that for all systems, the value of reactivity $r(\boldsymbol{x}_s)$ varies along the attractor. We have exploited this variability to design the Coupling When Needed strategy.

Supplementary Note 6. COMPARISON WITH THE CASE OF ON/OFF COUPLING

As we have discussed in the main text, for a particular choice of parameters, our CWN strategy is reduced to ON/OFF coupling, similar to the work of Refs.[9–13]. In what follows we present a comparison between our CWN strategy and these previous works.

One of the first papers to study an on-off 'blinking' coupling strategy is Ref.[9]. This paper considered an on/off coupling occurring on a time scale that is much faster than that of an individual oscillator, which is in contrast with our work where the variations are on the same time scale as those of the oscillators. The case of fast switching is also the focus of Ref.[10].

Reference[12] implemented a switching coupling strategy $\sigma(t) = \sigma_1 + \frac{\sigma_1+\sigma_2}{2}(\text{sign}(\cos(\omega t)) + 1)$ for a system of two coupled Rössler oscillators. The coupling strength switches periodically between two values σ_1 and σ_2, which are outside the range of synchronous coupling predicted by the MSF, but their average is inside the interval. Reference[13] used the same periodic switching law as Ref.[12] and showed that the coupled modified Hindmarsh–Rose system can be synchronized if one of the coupling values is outside the range predicted by the MSF. Reference[14] implemented a continuous periodic coupling

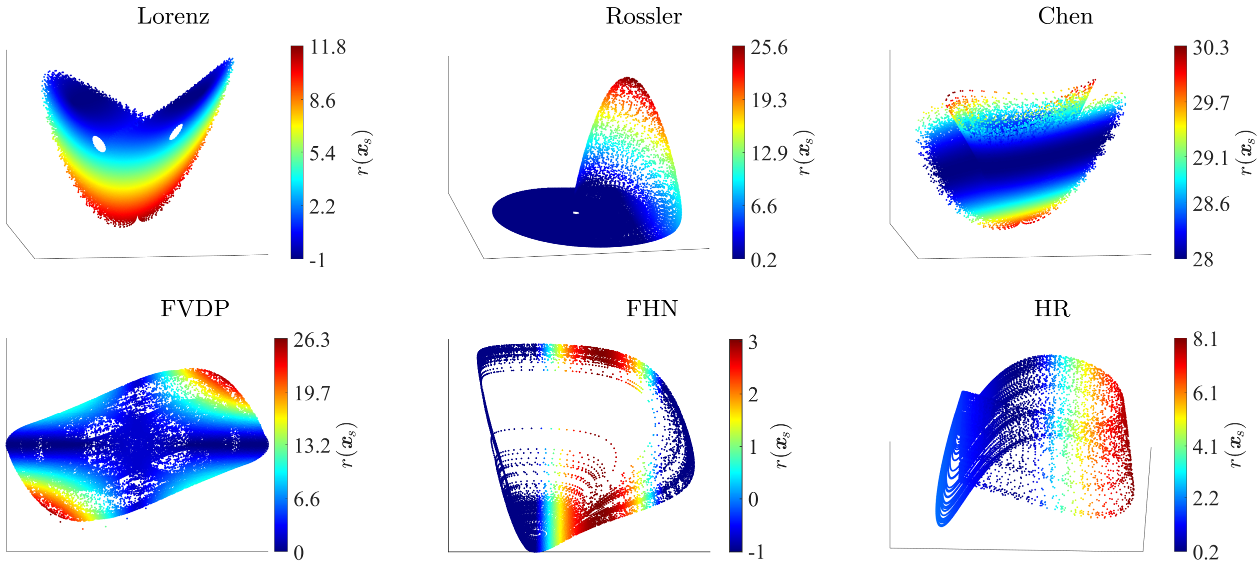

Supplementary Fig. 2. **The reactivity $r(\boldsymbol{x}_s)$ for different attractors.**

strategy in the form of $\sigma(t) = \sigma_0(1 - \sin(\omega t))$. The authors showed that the upper bounds of the bounded range of the synchronous coupling strength predicted by the MSF approach could be increased via this coupling strategy. However, the framework proposed in Ref.[14] was unable to shift the lower bound significantly. In contrast to Refs.[12,13], we show that by using our switching strategy, a system of coupled oscillators can synchronize even if the two values of the switching laws and their average are all outside the range of synchronous coupling predicted by the MSF. As we will see, in contrast to Ref.[14], our framework significantly enlarges the synchronous range of the coupling strength in both the lower and the upper bound.

In the rest of this section, we provide a detailed comparison between our state-dependent coupling strategy with the on/off coupling strategy of Ref.[11]. We take the same Rössler oscillator used in[11] and set our parameters $\alpha = \gamma = 0$ and $\beta = 0.2$ in

$$\sigma(t) = \begin{cases} \bar{\sigma}\frac{1-\gamma(1-\tau)}{\tau}, & r(\bar{\boldsymbol{x}}(t)) > \beta, \\ \\ \bar{\sigma}\gamma, & r(\bar{\boldsymbol{x}}(t)) \le \beta. \end{cases} \tag{S17}$$

and

$$\sigma(t) = \begin{cases} \bar{\sigma}\alpha, & r(\bar{\boldsymbol{x}}(t)) > \beta \\ \\ \bar{\sigma}\dfrac{1-\tau\alpha}{1-\tau}, & r(\bar{\boldsymbol{x}}(t)) \le \beta \end{cases} \tag{S18}$$

which results $\tau = 0.1307 \pm 0.0105$ over $0 \le \bar{\sigma} \le 5$. We note here that by setting $\alpha = \gamma = 0$, the general coupling strategy proposed in the main text is transformed into an on/off coupling strategy.

On the other hand, the on/off coupling presented in[11] is

$$\tilde{\sigma}(t) = \begin{cases} \sigma_{on}, & MT \le t < (M+\theta)T \\ 0, & (M+\theta)T \le t < (M+1)T \end{cases}, \tag{S19}$$

where $M = 1, 2, 3, \ldots$, the period of the coupling $T > 0$ and the fractions of the times the coupling is on $0 \le \theta \le 1$ are tunable parameters. For a fair comparison, we set $\theta = \tau$ and $\sigma_{on} = \bar{\sigma}/\theta$. Based on our simulations, we have seen that the widest interval of synchronization for $\bar{\sigma}$ is observed for small T. We thus set $T = 0.1$. The coupling matrix and the local dynamics and the coupling matrix are

$$\boldsymbol{x} = \begin{bmatrix} x \\ y \\ z \end{bmatrix}, \quad \boldsymbol{F}(\boldsymbol{x}) = \begin{bmatrix} -y - x \\ x + 0.2y \\ 0.2 + (x-9)z \end{bmatrix}, \quad H = \begin{bmatrix} 1 & 0 & 0 \\ 0 & 0 & 0 \\ 0 & 0 & 0 \end{bmatrix}, \tag{S20}$$

and we set the Laplacian matrix to be

$$L = \begin{bmatrix} -1 & 0 & 1 & 0 \\ 1 & -2 & 1 & 0 \\ 0 & 1 & -1 & 0 \\ 1 & 1 & 1 & -3 \end{bmatrix}. \tag{S21}$$

Supplementary Fig. 3 shows the synchronization error E vs $\bar{\sigma}$ for three different coupling strategies: 1- the constant coupling $\sigma = \bar{\sigma}$ (blue curve), 2- our proposed coupling strategy CWN in Eqs. (S17) and (S18) (yellow curve), and 3- the on/off coupling strategy from Ref.[11] (red curve). As can be seen, the CWN strategy is successful in significantly increasing the lower bound of the synchronous average coupling, compared to the case of constant coupling, while the method of[11] actually reduces it.

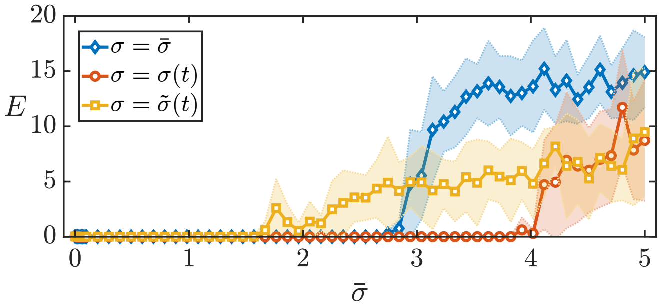

Supplementary Fig. 3. **Synchronizaton Error E as the average coupling strength $\bar{\sigma}$ is varied for three coupling strategies:** 1- constant coupling $\sigma = \bar{\sigma}$ in blue, 2- our proposed CWN coupling strategy from Eqs. (S17) and (S18) in red, and 3- the on/off coupling strategy proposed in[11] in yellow which is not a special case of our proposed CWN strategy.

Supplementary Note 7. LINEAR CONSENSUS PROBLEM

In this section, we discuss the consensus problem in which N systems/agents are dynamically coupled in order to reach a common state or ‘agreement’. Specifically, we consider the single integrator consensus problem, which consists of finding the appropriate protocols $u_i(t), i = 1, \dots, N$, such that the scalar states of the system $x_i(t)$ reach the consensus state following the set of equations,

$$\dot{x}_i(t) = u_i(t), \quad i = 1, \dots, N. \tag{S22}$$

It has been shown, e.g., see[15], that a simple protocol in the form

$$u_i = A_{ij}(x_j - x_i) \tag{S23}$$

is sufficient for the states $x_i(t)$ in Eq. (S22) to reach an agreement. Here, $A = [A_{ij}] \in \mathbb{R}^{N \times N}$ is the adjacency matrix, with non-negative entries. The graph corresponding to this adjacency matrix A has at least one directed spanning tree. Hence, the consensus problem can be rewritten in the compact form,

$$\dot{\boldsymbol{x}}(t) = L\boldsymbol{x}(t) \tag{S24}$$

where L is the Laplacian matrix corresponding to the adjacency matrix A, and $\boldsymbol{x} = [x_1 \ \ x_2 \ \ \dots \ \ x_N]^\top$. By the assumptions, the Laplacian matrix L has a single eigenvalue equal to zero and the corresponding right eigenvector is $\mathbf{1} = [1 \ \ 1 \ \ \dots \ \ 1]^\top$. We follow the procedure in the main manuscript and find the orthogonal transformation $\tilde{V} \in \mathbb{R}^{N \times (N-1)}$ with columns all orthogonal to the vector $\mathbf{1}$ (and to one another). By application of the transformation $\tilde{V}$, we can isolate the transverse dynamics,

$$\dot{\boldsymbol{x}}_\perp(t) = \hat{L}\boldsymbol{x}_\perp(t), \tag{S25}$$

where $\boldsymbol{x}_\perp(t) = \tilde{V}^\top \boldsymbol{x}(t) \in \mathbb{R}^{(N-1)}$, and the matrix $\hat{L} = \tilde{V}^\top L \tilde{V} \in \mathbb{R}^{(N-1)\times(N-1)}$. The matrix $\hat{L}$ has the same spectrum as the original Laplacian matrix L, except for the single eigenvalue zero. Since there are no internal dynamics ($F(x_i(t)) = 0$), the transverse reactivity, similar to Eq. (5) of the main manuscripts, turns into the largest eigenvalue of the matrix $\hat{Z} = (\hat{L}^\top + \hat{L})/2$, i.e.,

$$r = e_1(\hat{Z}) = e_1\left(\frac{\hat{L}^\top + \hat{L}}{2}\right). \tag{S26}$$

Thus, depending on the sign of r, the critical probability defined in Methods of the main manuscript becomes

$$\mu = \begin{cases} 1, & r > 0 \\ 0, & r < 0. \end{cases} \tag{S27}$$

Supplementary Note 8. CONTROL OF DRAGON KINGS

A “dragon king” is a rare but extreme event, for which the distribution of the size of the events follows a scale-free probability distribution. In the presence of noise or small parametric mismatches, the set of Eqs. (1) of the main text may converge on an the approximately synchronized solution, with the possible occurrence of large resynchronization, bursts away from the synchronization manifold[16], when in the presence of ‘attractor bubbling’. Bubbling is characterized by long excursions of high-quality synchronization interspersed by brief desynchronization events, whereby high-quality synchronization usually means that the maximum observed norm of the transverse perturbations remains small, within a few percent of the characteristic dimensions of the attractor. More specifically, bubbling arises in the synchronization dynamics when a significant increase in the norm of the transverse perturbations is seen in a short window of time. Within this context, dragon king events are particularly large but rare desynchronization bursts.

We apply our theory of reactivity to controlling attractor bubbling in the synchronization dynamics, which was originally reported in[17]. Reference[17] considered a master-slave configuration for two coupled chaotic circuits and showed both numerically and experimentally that bubbling occurs when the average trajectory is close to the origin. The authors of[17] then proposed a coupling scheme that uses strong coupling when the average trajectory is ‘near’ the origin and weak coupling when the average trajectory is ‘far’ from the origin, and chose the threshold for being near the origin somewhat arbitrarily. It was also mentioned in the conclusions of[17] that it is not believed that there is any general way to identify in which regions of the attractor one should increase the coupling to prevent bubbling in general and dragon kings in particular.

In what follows we provide an interpretation of and an explanation for the proposed coupling scheme of[17] in terms of reactivity. The state vector is $\boldsymbol{x} = [V_1 \ V_2 \ I]^\top$ and the local dynamics of each circuit is described by the function,

$$\boldsymbol{F}(\boldsymbol{x}) = \begin{bmatrix} V_1/R_1 - g(V_1 - V_2) \\ g(V_1 - V_2) - I \\ V_2 - R_4 I \end{bmatrix}, \tag{S28}$$

where $g(V) = V/R_2 + I_r[\exp(\alpha_f V) - \exp(-\alpha_r V)]$. The parameters are $R_1 = 1.3$, $R_2 = 3.44$, $R_4 = 0.193$, $I_r = 22.5(10^{-6})$, and $\alpha_r = \alpha_f = 11.6$. We set the coupling strength to be $\sigma = 4.4$ and the Laplacian matrix to be

$$L = \begin{bmatrix} 0 & 0 \\ 1 & -1 \end{bmatrix}. \tag{S29}$$

With this specific choice of the Laplacian matrix, the state vector that describes the motion parallel to the synchronization manifold, $\boldsymbol{x}_1 = \boldsymbol{x}_2$, is

$$\boldsymbol{x}_\parallel(t) = \boldsymbol{x}_s(t) = \frac{\boldsymbol{x}_1(t) + \boldsymbol{x}_2(t)}{2}. \tag{S30}$$

The state vector that describes the motion transverse to the synchronization manifold is

$$\boldsymbol{x}_\perp = \frac{\boldsymbol{x}_1(t) - \boldsymbol{x}_2(t)}{2}. \tag{S31}$$

Supplementary Fig. 4 shows the values of reactivity for the points $\boldsymbol{x}_s$ on the chaotic attractor for the dynamics of an uncoupled circuit obeying $\dot{\boldsymbol{x}}_s = \boldsymbol{F}(\boldsymbol{x}_s)$. We clearly see that the area close to the origin has a higher (and positive) reactivity while the points on the two scrolls have lower (and negative) reactivity. This results in a higher tendency for the norm of $\boldsymbol{x}_\perp$ to increase when $\boldsymbol{x}_\parallel$ is close to the origin.

We now compare the case of constant coupling, $\sigma = \bar{\sigma} = 4.4$ and the time-varying coupling from Eq. (S17). in which we set the parameters $\gamma = 0.9$ and $\beta = -0.192$ which results in $\tau \approx 0.2610$. Based on the values of reactivity in Supplementary Fig. 4, the value of β is selected such that the coupling strength is lower in the scrolls (the blue region) and is higher near the origin (the red region.)

Following[17], we set the coupling matrix for the time-varying coupling strategy, $\sigma = \sigma(t)$, to be time-varying as well with the difference that we use the transverse reactivity to determine when to switch:

$$H(t) = \begin{cases} \begin{bmatrix} 1 & 0 & 0 \\ 0 & 1 & 0 \\ 0 & 0 & 0 \end{bmatrix}, & r(\boldsymbol{x}_\parallel(t)) > \beta \\ \\ \begin{bmatrix} 0 & 0 & 0 \\ 0 & 1 & 0 \\ 0 & 0 & 0 \end{bmatrix}, & r(\boldsymbol{x}_\parallel(t)) \le \beta, \end{cases} \tag{S32}$$

while the coupling matrix H is constant for the constant coupling case, $\sigma = \bar{\sigma}$, with

$$H = \begin{bmatrix} 0 & 0 & 0 \\ 0 & 1 & 0 \\ 0 & 0 & 0 \end{bmatrix}. \tag{S33}$$

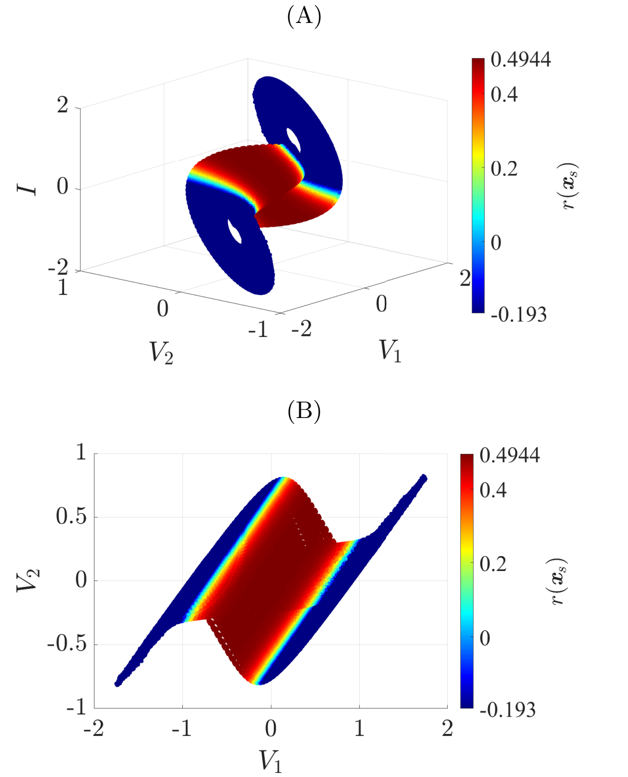

Supplementary Fig. 4. **Reactivity of the points on the chaotic circuit attractor $r(\boldsymbol{x}_s)$.** Panel (A) shows the 3D plot and panel (B) shows the 2D plot in the V_1V_2 plane.

We set the level of the added white Gaussian noise to be 0.02 and we use the Henon method[18] to integrate the noisy ODE. Supplementary Fig. 5(A) shows that the norm of the transverse motion does not significantly increase under the time-varying coupling from Eq. (S17), while several surges are seen when the coupling is constant. A particular large event is visualized in Supplementary Fig. 5(B), which also shows the values of the reactivity of the parallel motion at that time. It is clear that the transverse motion begins to leave the synchronization manifold about the time when the reactivity is largest (dark red.)

Our approach provides a practical way to set the threshold for what in[17] is defined as 'near the origin'. There are two main advantages of our work. The first one is that it is quantitative, as it provides an approach to compute the threshold; the second one is that it is general, as it works for any system, not just one where the unstable fixed points are known. We believe that the coupling scheme proposed in[17] is a specific case of our general coupling scheme.

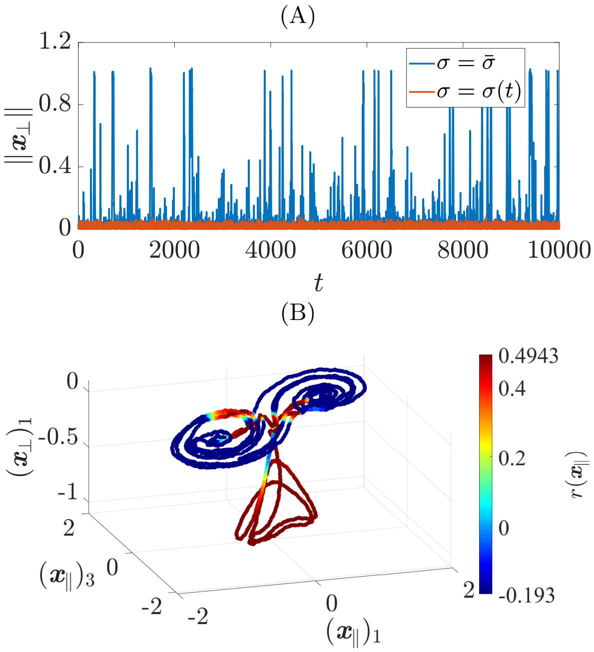

Supplementary Fig. 5. **The occurrence of bubbling in the presence of noise.** Panel (A) shows the norm of the transverse perturbations for the constant coupling $\sigma = \bar{\sigma}$ and time-varying coupling $\sigma(t)$ from Eq. (S17). Panel (B) visualizes the dynamics in the space with axes $(\boldsymbol{x}_\parallel)_1, (\boldsymbol{x}_\parallel)_3, (\boldsymbol{x}_\perp)_1$, and displays the jump seen at time $t = 1498.2$ in panel (A) for the case of constant coupling.

Supplementary Note 9. EXAMPLES WITH DIFFERENT DYNAMICS

In this section, we show the effectiveness of our proposed CWN strategy for different dynamics than presented in the main paper. We take the same 4-node topology in the main text with the Laplacian

$$L = \begin{bmatrix} -1 & 0 & 1 & 0 \\ 1 & -2 & 1 & 0 \\ 0 & 1 & -1 & 0 \\ 1 & 1 & 1 & -3 \end{bmatrix}. \tag{S34}$$

We vary $\bar{\sigma}$ and compute the synchronization error E and the synchronization energy $\mathcal{E}$ (both are defined in the main manuscript) when

1. the coupling is constant, $\sigma = \bar{\sigma}$, and

2. the coupling is time-varying, Eq. (S17).

Examples are provided with different choices of the chaotic local dynamics such as the Hindmarsh–Rose neuron model, the FitzHugh-Nagumo neuron model and the forced Van Der Pol oscillator.

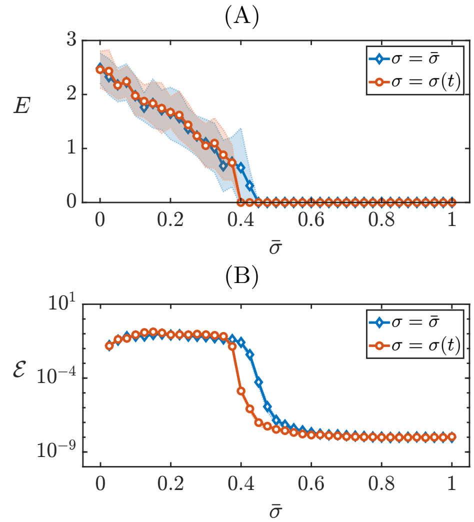

Supplementary Fig. 6. **The HR model.** the synchronization error E (A) and the synchronization energy $\mathcal{E}$ (B) versus the average coupling strength $\bar{\sigma}$. The data for both panels are averaged over 20 realizations initiated from randomly chosen initial conditions. The shaded backgrounds show the standard deviation of the plotted data.

A. The Hindmarsh–Rose neuron model

Here, we take the local dynamics to be the Hindmarsh–Rose (HR) model of neural activity. The local dynamics $\boldsymbol{F}$ and the coupling matrix H are taken to be

$$\boldsymbol{x} = \begin{bmatrix} x \\ y \\ z \end{bmatrix}, \quad \boldsymbol{F}(\boldsymbol{x}) = \begin{bmatrix} y + 3x^2 - x^3 - z + 3.2 \\ 1 - 5x^2 - y \\ -0.006z + 0.024(x + 1.6) \end{bmatrix}, \quad H = \begin{bmatrix} 1 & 0 & 0 \\ 0 & 0 & 0 \\ 0 & 0 & 0 \end{bmatrix}. \tag{S35}$$

For this particular choice of parameters, the local dynamics $\dot{\boldsymbol{x}}(t) = \boldsymbol{F}(\boldsymbol{x}(t))$ has a chaotic attractor[7]. We set $\beta = 1$ and $\gamma = 0.01$ in Eq. (S17) for the time-varying coupling strategy.

Supplementary Fig. 6(A) shows the reduction of 11% in the average coupling $\bar{\sigma}$ (from 0.45 reduced to 0.4) when the time-varying coupling strategy is implemented. It is also clear in Supplementary Fig. 6(B) that the synchronization energy $\mathcal{E}$ is also smaller when the coupling is time-varying.

B. Forced Van Der Pol oscillator

Here, we take the local dynamics to be the forced Van Der Pol (VDP). The local dynamics $\boldsymbol{F}$ and the coupling

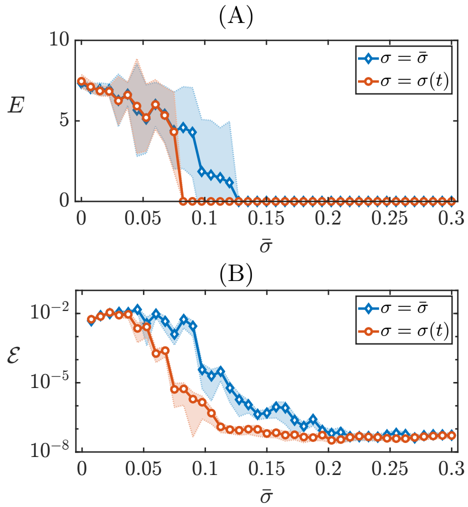

Supplementary Fig. 7. **The Forced VDP system:** the synchronization error E (A) and the synchronization energy $\mathcal{E}$ (B) versus the average coupling strength $\bar{\sigma}$. The data for both panels are averaged over 20 realizations initiated from randomly chosen initial conditions. The shaded backgrounds show the standard deviation of the plotted data.

matrix H are taken to be

$$\boldsymbol{x} = \begin{bmatrix} x \\ y \end{bmatrix}, \quad \boldsymbol{F}(\boldsymbol{x}) = \begin{bmatrix} y \\ -x + 3(1-x^2)y + 15\sin(4.065t) \end{bmatrix}, \quad H = \begin{bmatrix} 0 & 0 \\ 0 & 1 \end{bmatrix}. \tag{S36}$$

For this particular choice of parameters, the local dynamics $\dot{\boldsymbol{x}}(t) = \boldsymbol{F}(\boldsymbol{x}(t))$ has a chaotic attractor[7]. We set $\beta = 3.24$ and $\gamma = 0.6$ in Eq. (S17) for the time-varying coupling strategy.

Supplementary Fig. 7(A) shows the reduction of 38% in the average coupling $\bar{\sigma}$ (from 0.18 reduced to 0.11) when the time-varying coupling strategy is implemented. It is also clear in Supplementary Fig. 7(B) that the synchronization energy $\mathcal{E}$ is also smaller when the coupling is time-varying.

C. FitzHugh–Nagumo neuron model

Here, we take the local dynamics to be the forced FitzHugh–Nagumo (FHN) model. The local dynamics $\boldsymbol{F}$ and the coupling matrix H are taken to be

$$\boldsymbol{x} = \begin{bmatrix} x \\ y \end{bmatrix}, \qquad H = \begin{bmatrix} 1 & 0 \\ 0 & 0 \end{bmatrix}, \quad \boldsymbol{F}(\boldsymbol{x}) = \begin{bmatrix} x(x-1)(1-10x) - y + \frac{0.1}{2\pi f}\cos(2\pi f t) \\ x \end{bmatrix}, \tag{S37}$$

where $f = 0.129$. For this particular choice of parameters, the local dynamics $\dot{\boldsymbol{x}}(t) = \boldsymbol{F}(\boldsymbol{x}(t))$ has a chaotic attractor[19]. We set $\beta = 1.61$ and $\gamma = 0.158$ in Eq. (S17) for the time-varying coupling strategy.

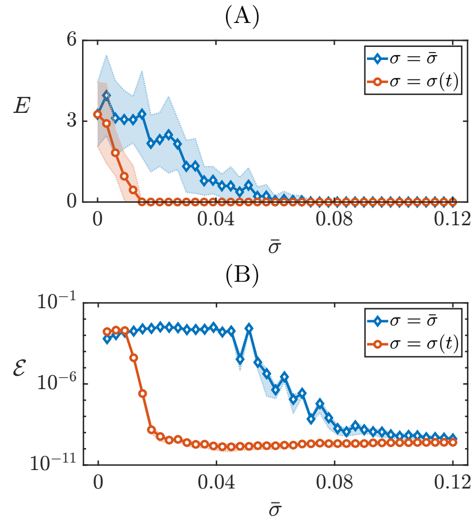

Supplementary Fig. 8. **The FHN system:** the synchronization error E (A) and the synchronization energy $\mathcal{E}$ (B) versus the average coupling strength $\bar{\sigma}$. The data for both panels are averaged over 20 realizations initiated from randomly chosen initial conditions. The shaded backgrounds show the standard deviation of the plotted data.

Supplementary Fig. 8(A) shows the reduction of 76% in the average coupling $\bar{\sigma}$ (from 0.075 reduced to 0.018) when the time-varying coupling strategy is implemented. It is also clear in Supplementary Fig. 8(B) that the synchronization energy $\mathcal{E}$ is also smaller when the coupling is time-varying.

Supplementary Note 10. SYNCHRONIZATION ENERGY COMPARISON

In this section, we plot the synchronization error vs energy from the simulation data shown in Fig. 2 A of the main manuscript corresponding to the case of 4 coupled Lorenz oscillators. From Supplementary Fig. 9, we cannot see a significant difference in the synchronization error when the energy for the constant coupling and the CWN are the same. However, this statement does not consider the effect of the average coupling strength $\bar{\sigma}$; thus we have decided to show $\bar{\sigma}$ as colors. Now, for the same color ($\bar{\sigma}$), we see that both energy and the synchronization error are higher in the case of constant coupling in comparison to the CWN.

Supplementary Note 11. ENERGY EFFICIENCY

In this section, we provide examples of the energy efficiency of the synchronization dynamics. We use the same 4-node topology with the Laplacian matrix from Eq. (S34) and set the local dynamics and the coupling

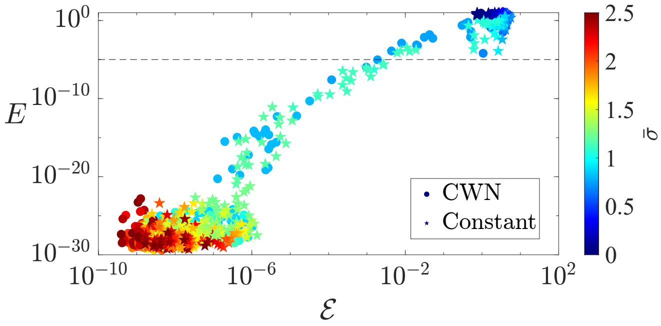

Supplementary Fig. 9. **The synchronization error E vs the synchronization energy $\mathcal{E}$ of coupled Lorenz oscillators.** The colors show the average coupling strength $\bar{\sigma}$. The data corresponding to the CWN and constant coupling strategies are shown in circles and stars, respectively. The dashed black line shows the threshold of $E = 10^{-5}$ that may be considered the boundary for the occurrence of synchronization. The plotted data corresponds to the simulation results from Fig. 2A of the main manuscript.

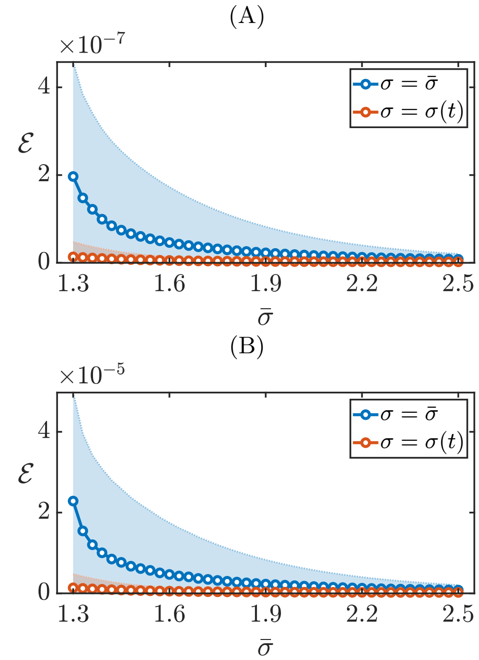

Supplementary Fig. 10. **Synchronization energy $\mathcal{E}$ vs. the average coupling strength $\bar{\sigma}$.** For each $\bar{\sigma}$, the average $\mathcal{E}$ is plotted over the set of 20 random initial conditions in Eq. (S40). The shaded background shows the standard deviation. In panel (A), the norm of the initial perturbations is $\kappa = 10^{-6}$, and in panel (B), it is $\kappa = 10^{-4}$.

matrix to be as in (S9). For this choice of network topology, the local dynamics, and the coupling matrix, the threshold for synchronization in terms of the coupling strength is $\sigma^{A\to S} = 1.3$. We vary $\bar{\sigma}$ in the interval [1.3 2.5] in which the system in

$$\dot{\boldsymbol{x}}_i(t) = \boldsymbol{F}(\boldsymbol{x}_i(t)) + \sigma(t)\sum_{j=1}^{N} L_{ij} H \boldsymbol{x}_j(t), \quad i = 1, \dots, N, \tag{S38}$$

will synchronize with $\sigma(t) = \bar{\sigma}$. We compare the energy required for synchronization

$$\mathcal{E} = \frac{1}{N}\sum_{i=1}^{N} \frac{1}{t_f - t_0} \int_{t_0}^{t_f} \|\boldsymbol{u}_i(t)\|_2 dt \tag{S39}$$

in the two cases of constant coupling $\bar{\sigma}$ and the time-varying coupling strength from Eq. (S17).

We set $t_0 = 0$ and $t_f = 200s$ in Eq. (S39). The parameters in Eq. (S17) are fixed at $\beta = 0.5$, $\gamma = 0.16$. We randomly pick 20 points from the attractor, $\boldsymbol{s}_0$, and 20 vectors $\delta\boldsymbol{X}$ with the unit norm and entries randomly chosen from a normal distribution, for generating the initial perturbations. Namely, for each pair of randomly generated $(\boldsymbol{s}_0, \delta\boldsymbol{X})$, we set the initial condition for Eq. (S38) as

$$\begin{bmatrix} \boldsymbol{x}_1(0) \\ \boldsymbol{x}_2(0) \\ \vdots \\ \boldsymbol{x}_N(0) \end{bmatrix} = \mathbf{1}_N \otimes \boldsymbol{s}_0 + \kappa \delta \boldsymbol{X} \tag{S40}$$

where $\mathbf{1}_N$ is a vector of all ones with size N and the tunable parameter $\kappa > 0$ defines the norm of the perturbation about the synchronous solution. The initial conditions generated from Eq. (S40) are kept the same for all values of $\bar{\sigma}$. We simulate Eq. (S38) with either $\sigma(t) = \bar{\sigma}$ or with $\sigma(t)$ from Eq. (S17) and plot the energy $\mathcal{E}$ as $\bar{\sigma}$ is varied.

Supplementary Fig. 10 shows the advantage of implementing the time-varying coupling strategy in achieving synchronization by the use of less energy. The figure also demonstrates that when $\bar{\sigma}$ is close to $\sigma^{A\to S}$, more energy is required since the MLE is larger. This, in turn, implies that the transient regime of the transverse dynamics will take longer to dissipate, hence synchronization will be achieved at later times, causing the energy required for synchronization to increase.

Supplementary Note 12. EXAMPLE LORENZ FOR S $\to$ A TRANSITION

We study in more detail the switching coupling law in Eq. (S18). We consider the case of Lorenz oscillators coupled in the z-variable. The MSF threshold for synchronization corresponding to the S $\to$ A transition is $\sigma^{S\to A} Re(\lambda_2) \approx -9.23$ as reported in[7]. Here, we wish to see how larger we may set $\bar{\sigma} Re(\lambda_2)$ than the MSF threshold (larger than 9.23 in magnitude) and still observe synchronization. To this end, we vary α and β in Eq. (S18) and find the largest

$$\%\ \text{MSF threshold } S \to A = 100\frac{\bar{\sigma}}{\sigma^{S\to A}}.$$

Supplementary Fig. 11 shows the % MSF threshold

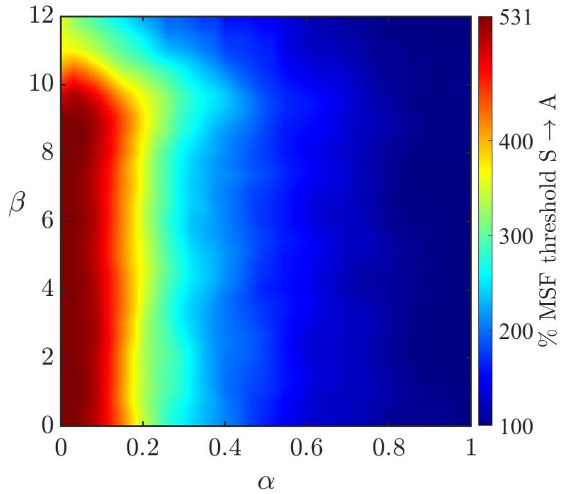

Supplementary Fig. 11. **Effect of the parameter settings on the performance of the control strategy in Eq.** (S18)**.** % MSF threshold as the parameters α and β in Eq. (S18) are varied. The network topology is given by the Laplacian matrix in Eq. (S34).

$S \to A$ as a function of α and β for the unweighted network with the Laplacian matix in Eq. (S34). We see that the switching law in Eq. (S18) can successfully synchronize the network for an average coupling as large as 530% of the critical coupling strength corresponding to the MSF threshold. This significant increase in $\bar{\sigma}$ is achieved by lowering the coupling in the highly reactive region of the attractor and by increasing it in the region of low reactivity.

Supplementary Note 13. DETAILS ON THE OPTO-ELECTRONIC OSCILLATOR EXPERIMENT

The experimental network consists of two opto-electronic oscillators similar to those described in Refs.[20–25]. A schematic of our opto-electronic oscillator network is shown in Supplementary Fig. 12. Constant intensity light from a laser diode passes through an integrated intensity modulator, which implements a sinusoidal nonlinearity, $\mathcal{I}(x) = \cos^2(x)$, where $x = \pi v/2V_\pi$ is the dynamical variable, v is the voltage applied to the modulator, and V_ϕ is the half-wave voltage of the intensity modulator. The modulated light passes through a fiber delay line and is converted to an electrical signal by a photoreceiver. This electrical signal is digitized onto a field-programmable gate array (FPGA) by an analog-to-digital (ADC) converter. The coupling and low pass filtering are implemented digitally on the FPGA, and the filter output is converted to an electrical signal by a digital-to-analog converter (DAC), amplified, and applied to the RF port of the intensity modulator, completing the feedback loop.

In addition to the coupling efficiency, which was presented in the main text, we computed the energy efficiency of the opto-electronic oscillator experiment. The results are shown in Supplementary Fig. 13. The case of constant coupling strength is shown in blue, while the energy efficiency of our time-varying coupling strategy is shown in red. We see that the coupling energy of the time-varying coupling strategy is smaller or at worst approximately the same as the constant coupling for both the A → S and S → A transitions when the error is close to zero. We can not use the time-varying coupling strategy for values of $\bar{\sigma}$ near 2, because for this particular system, the reactivity is nearly constant across the entire attractor when $\bar{\sigma} \approx 2$.

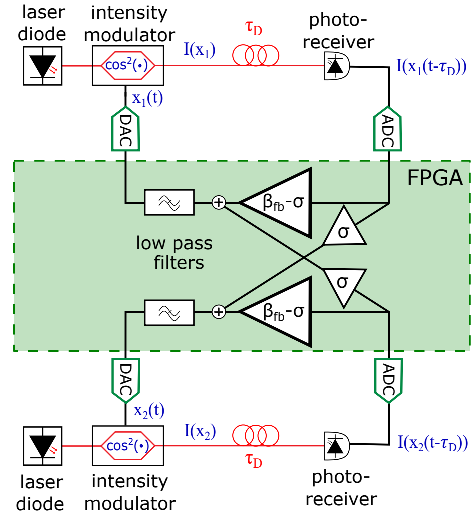

Supplementary Fig. 12. **Schematic depiction of the opto-electronic oscillator network.** The algorithm for controlling the time-dependent coupling strength $\sigma(t)$ is implemented in real time in the FPGA digital logic.

A. Real-time implementation of algorithm for determining $\sigma(t)$ for the opto-electronics experiment

The following details are adapted from the classic 1982 paper by Farmer[26]. The equations of motion of a system of coupled opto-electronic oscillators are given by a set of coupled delay differential equations:

$$\begin{aligned}\frac{d}{dt}x_i(t) = &-\frac{1}{T}x_i(t) + \frac{1}{T}\beta\cos^2(x_i(t-\tau)+\phi) \\ &+\frac{1}{T}\sigma\sum_j L_{ij}\cos^2(x_j(t-\tau)+\phi).\end{aligned} \tag{S41}$$

where T is the filter time constant, β determines the round trip gain, τ gives the time delay, and σ gives the coupling strength. The synchronous solution is given by

$$\frac{d}{dt}s(t) = -\frac{1}{T}s(t) + \frac{1}{T}\beta\cos^2(s(t-\tau)+\phi). \tag{S42}$$

Delay systems are technically infinite dimensional systems since the state of the system at time t depends on

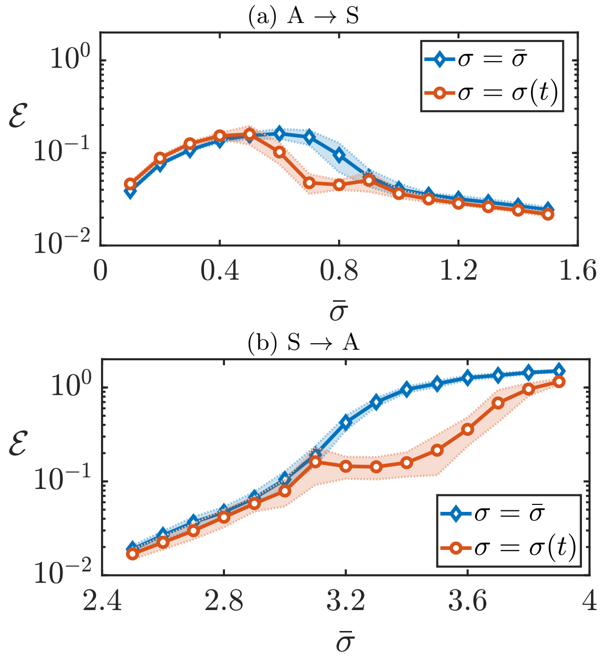

Supplementary Fig. 13. **Energy efficiency of the opto-electronic oscillator network.** The energy is plotted against the average coupling strength $\bar{\sigma}$ for the transitions (a) from asynchrony to synchrony and (b) synchrony to asynchrony. The blue (red) red curves show the constant (time-varying) coupling strategies. The shading shows the standard deviation.

the prior state of the system over the continuous interval $[t-\tau, t)$[26]. In practice, however, the delay system given in Eq. (S41) has an effective finite dimension with an upper limit that is determined by τ/T[27]. T is the low pass filter time constant and sets the time scale on which the fastest dynamics can occur. So if one divides the delay period τ into chunks of order T (say $T/5$)), one can effectively specify the entire span $[t-\tau, t)$ using a finite number of variables. Using this, we can write down an effective Jacobian, enabling computations of quantities such as the transverse reactivity as we show below.

The simplest way to do this is to do an Euler discretization of Eq. (S41):

$$\begin{aligned} x_i[n+1] = (1-\frac{\Delta t}{T})x_i[n] + \frac{\Delta t}{T}\{F(x_i[n-k]) \\ +\sigma \sum_j L_{ij} G(x_j[n-k])\} \end{aligned} \tag{S43}$$

where we have chosen the discrete time step Δt such that $k \equiv \tau/\Delta t$ is an integer and represents the delay in the number of time steps. Here, $\mathbf{F}(x) \equiv \beta \cos^2(x_i(t-\tau)+\phi)$ and $\mathbf{G}(x) \equiv \cos^2(x_i(t-\tau)+\phi)$, but the notation is general. Similarly, the synchronous solution in Eq. (S42) becomes

$$s[n+1] = (1-\frac{\Delta t}{T})s[n] + \frac{\Delta t}{T}F(s[n-k]). \tag{S44}$$

By linearizing Eq. (S43), the dynamics of the perturbations about the synchronous solution (i.e., $x_i[n] \to s[n] + \delta x_i[n]$) is described by

$$\begin{aligned} \delta x_i[n+1] =& (1-\frac{\Delta t}{T})\delta x_i[n] \\ &+ \frac{\Delta t}{T}\{dF(s[n-k])\delta x_i[n-k] \\ &+ \sigma \sum_j L_{ij} dG(s[n-k])\delta x_j[n-k]\} \end{aligned} \tag{S45}$$

Them, Eq. (S45) is rewritten in matrix form:

$$\begin{aligned} \begin{bmatrix} \delta x_i[n+1] \\ \delta x_i[n] \\ \delta x_i[n-1] \\ \vdots \\ \delta x_i[n+1-k] \end{bmatrix} =& \begin{bmatrix} (1-\Delta t/T) & 0 & 0 & \dots & 0 & \frac{\Delta t}{T} dF(s[n-k]) \\ 1 & 0 & 0 & \dots & 0 & 0 \\ 0 & 1 & 0 & \dots & 0 & 0 \\ 0 & 0 & 1 & \dots & 0 & 0 \\ \vdots & \vdots & \vdots & \dots & \vdots & \vdots \\ 0 & 0 & 0 & \dots & 1 & 0 \end{bmatrix} \begin{bmatrix} \delta x_i[n] \\ \delta x_i[n-1] \\ \delta x_i[n-2] \\ \vdots \\ \delta x_i[n-k] \end{bmatrix} \\ &+\sigma \sum_j L_{ij} \begin{bmatrix} 0 & 0 & 0 & \dots & 0 & \frac{\Delta t}{T} dG(s[n-k]) \\ 0 & 0 & 0 & \dots & 0 & 0 \\ 0 & 0 & 0 & \dots & 0 & 0 \\ 0 & 0 & 0 & \dots & 0 & 0 \\ \vdots & \vdots & \vdots & \dots & \vdots & \vdots \\ 0 & 0 & 0 & \dots & 0 & 0 \end{bmatrix} \begin{bmatrix} \delta x_j[n] \\ \delta x_j[n-1] \\ \delta x_j[n-2] \\ \vdots \\ \delta x_j[n-k] \end{bmatrix} \end{aligned} \tag{S46}$$

Defining $\delta \boldsymbol{x}_i[n] \equiv [\delta x_i[n], \delta x_i[n-1], \dots, \delta x_i[n-k]]^T$, we have

$$\delta \boldsymbol{x}_i[n+1] = \mathbf{A}_s[n]\delta \boldsymbol{x}_i[n] + \sigma \sum_j L_{ij} \mathbf{B}_s[n] \delta \boldsymbol{x}_j[n], \tag{S47}$$

where $\mathbf{A}_s$ is the first matrix in Eq. (S46) denoting the effect of the local dynamics and $\mathbf{B}_s$ is the second matrix in Eq. (S46) denoting the effect of the coupling. Now, Eq. (S47) is in the same form as the equations for perturbations in the main text. By stacking all $\delta \boldsymbol{x}_i$ vectors on top of each other to form $\delta \boldsymbol{X} = [\delta \boldsymbol{x}_1^\top \ \cdots \delta \boldsymbol{x}_N^\top]^\top$. We then remove the directions parallel to the synchronization manifold by the transformation $V \otimes I$ to obtain the transverse perturbation vector $\delta \hat{\boldsymbol{X}}$ where the dynamics is described by

$$\begin{aligned} \delta \boldsymbol{X}[n+1] = &\left(I_{N-1} \otimes \mathbf{A}_s[n]\right) \delta \boldsymbol{X}[n] \\ &+ \sigma \left(L^\perp \mathbf{B}_s[n]\right) \delta \boldsymbol{X}[n], \end{aligned} \tag{S48}$$

where $L^\perp = V^\top L V$. Now Eq. (S48) in the same form as Eq. (S2), so we carry on calculating the reactivity of this equation online and using it for the time-varying coupling strategy. Reference[5] has defined the reactivity associated with a linear discrete-time system in the form $\boldsymbol{x}_{k+1} = A \boldsymbol{x}_k$ as $r = \sigma_1(A) - 1$ where $\sigma_1(\cdot)$ returns the largest singular value of the matrix in its argument.

B. Largest singular value of the Z matrix

The key matrix in the computation of the reactivity is $\hat{\mathbf{Z}}$:

$$\hat{\mathbf{Z}}[n] \equiv I_{n-1} \otimes \mathbf{A}_s[n] + \bar{\sigma} L_{ij}^\perp \otimes \mathbf{B}_s[n]. \tag{S49}$$

The largest singular value of this matrix minus one determines the reactivity. For the bidirectionally coupled system of $N = 2$ nodes considered in the experiment, $L^\perp = -2$. The form of the matrices $\mathbf{A}$ and $\mathbf{B}$ allows us to analytically compute the singular values of the matrix $\hat{\mathbf{Z}}$, as we now show. The singular values of a matrix $\mathbf{M}$ are given by the square root of the eigenvalues of $\mathbf{M}\mathbf{M}^T$. We have that

$$\hat{\mathbf{Z}}[n] = \begin{bmatrix} A_{1,1} & 0 & 0 & \dots & 0 & A_{1,k-1} - 2\bar{\sigma} B_{1,k-1} & A_{1,k} = 2\bar{\sigma} B_{1,k} \\ 1 & 0 & 0 & \dots & 0 & 0 & 0 \\ 0 & 1 & 0 & \dots & 0 & 0 & 0 \\ 0 & 0 & 1 & \dots & 0 & 0 & 0 \\ \vdots & \vdots & \vdots & \dots & \vdots & \vdots & \vdots \\ 0 & 0 & 0 & \dots & 1 & 0 & 0 \end{bmatrix} \tag{S50}$$

and so

$$\hat{\mathbf{Z}}[n]\hat{\mathbf{Z}}^T[n] = \begin{bmatrix} Z_{1,1}^2 + Z_{1,k-1}^2 + Z_{1,k}^2 & Z_{1,1} & 0 & \dots & 0 & Z_{1,k-1} \\ Z_{1,1} & 1 & 0 & \dots & 0 & 0 \\ 0 & 0 & 1 & \dots & 0 & 0 \\ \vdots & \vdots & \vdots & \dots & \vdots & \vdots \\ Z_{1,k-1} & 0 & 0 & \dots & 0 & 1 \end{bmatrix}, \tag{S51}$$

where $Z_{i,j}$ refer to the matrix elements of $\hat{Z}$ in Eq. (S50). For the sake of simplicity, we define $C_{1,1} \equiv Z_{1,1}^2 + Z_{1,k-1}^2 + Z_{1,k}^2$.

The eigenvalues of $\hat{\mathbf{Z}}[n]\hat{\mathbf{Z}}^T[n]$ can be computed analytically in terms of the matrix elements of $\hat{Z}$. To compute the eigenvalues, we set the determinant of the matrix $\hat{\mathbf{Z}}[n]\hat{\mathbf{Z}}^T[n] - \lambda \mathcal{I}$ equal to zero:

$$\hat{\mathbf{Z}}[n]\hat{\mathbf{Z}}^T[n] - \lambda \mathcal{I} = \begin{bmatrix} C_{1,1} - \lambda & Z_{1,1} & 0 & \dots & 0 & Z_{1,k-1} \\ Z_{1,1} & 1-\lambda & 0 & \dots & 0 & 0 \\ 0 & 0 & 1-\lambda & \dots & 0 & 0 \\ \vdots & \vdots & \vdots & \dots & \vdots & \vdots \\ Z_{1,k-1} & 0 & 0 & \dots & 0 & 1-\lambda \end{bmatrix}. \tag{S52}$$

Laplace (cofactor) expansion reduces the determinant to:

$$\begin{aligned} det(\hat{\mathbf{Z}}[n]\hat{\mathbf{Z}}^T[n] - \lambda \mathcal{I}) &= (1-\lambda)^{k-3} \\ \times det &\left\{ \begin{bmatrix} C_{1,1} - \lambda & Z_{1,1} & Z_{1,k-1} \\ Z_{1,1} & 1-\lambda & 0 \\ Z_{1,k-1} & 0 & 1-\lambda \end{bmatrix} \right\} \end{aligned} \tag{S53}$$

and therefore we have

$$\begin{aligned} det(\hat{\mathbf{Z}}[n]\hat{\mathbf{Z}}^T[n] - \lambda \mathcal{I}) = (1-\lambda)^{k-2}\{&(C_{1,1} - \lambda)(1-\lambda) \\ &- Z_{1,1}^2 - Z_{1,k-1}^2\}. \end{aligned} \tag{S54}$$

There are $k-2$ degenerate eigenvalues equal to 1. The other two eigenvalues are given by the roots of the quadratic polynomial in curly brackets. The roots are

$$\lambda_\pm = \frac{C_{1,1} + 1 \pm \sqrt{(C_{1,1}+1)^2 - 4(C_{1,1} - Z_{1,1}^2 - Z_{1,k-1}^2)}}{2}. \tag{S55}$$

Therefore, the largest singular value of $\mathbf{Z}[n]$ is given by $\sigma_{max} = \sqrt{\lambda_+}$.

C. The reactivity and the threshold

The control scheme consists of comparing the reactivity to a threshold, called η at each time step. The reactivity is given by

$$r[n] = \sigma_{max}[n] - 1. \tag{S56}$$

Equation (S55) can be used to simplify the condition that $r[n] > \eta$:

$$\begin{aligned}
r[n] &> \eta \\
\sigma_{max}[n] - 1 &> \eta \\
\lambda_+[n] &> (\eta+1)^2 \\
\frac{C_{1,1}+1 \pm \sqrt{(C_{1,1}+1)^2 - 4(C_{1,1} - Z_{1,1}^2 - Z_{1,k-1}^2)}}{2} &> (\eta+1)^2 \\
(C_{1,1}+1)^2 - 4(C_{1,1} - Z_{1,1}^2 - Z_{1,k-1}^2) &> \{2(\eta+1)^2 - C_{1,1} - 1\}^2 \\
\{(\eta+1)^2 - 1\}C_{1,1} + Z_{1,1}^2 + Z_{1,k-1}^2 &> (\eta+1)^4 - (\eta+1)^2.
\end{aligned} \tag{S57}$$

The right-hand side is a constant, so it only needs to be evaluated once. Similarly, $Z_{1,1}^2$ is a constant. Evaluating this condition at each time step is more computationally efficient than building up $\mathbf{Z}$ and numerically computing its singular values. This is particularly important for the experimental control system, where timing matters.

Supplementary Note 14. DEFINITION OF SYNCHREACTIVITY FOR THE CASE THAT THE MASTER STABILITY FUNCTION IS NEGATIVE IN A BOUNDED RANGE OF ITS ARGUMENT

Here, we proceed under the assumption that the particular choice of the local dynamics $\boldsymbol{F}$ and of the coupling matrix H results in a master stability function (MSF) that is negative in a bounded range of its argument, $\sigma Re(\lambda_i)$. We select two arbitrary networks with Laplacian matrices L_A and L_B and assume they are both synchronizable. That is, $Re(\lambda_N)/Re(\lambda_2) < b/a$, where a and b are the MSF thresholds corresponding to the transition $A \to S$ and $S \to A$, respectively. We aim to compare the reactivity $r(\boldsymbol{x}_s)$ and the critical probability μ for these two networks. First, we focus on two cases:

1. the coupling strength σ is close to $\sigma^{A\to S}$,
2. the coupling strength σ is close to $\sigma^{S\to A}$.

In case 1, the definition of the syncreactivity we provided in the main text

$$\Xi = 1 - \frac{\xi}{Re(\lambda_2)} \geq 0, \tag{S58}$$

applies. The network with higher Ξ has larger $r(\boldsymbol{x}_s)$ and μ, i.e., if $\Xi^A > \Xi^B$, then $r^A(\boldsymbol{x}_s) \geq r^B(\boldsymbol{x}_s)$ and $\mu^A \geq \mu^B$.

In case 2, we set σ^A and σ^B such that $\sigma^A Re(\lambda_N^A) = \sigma^B Re(\lambda_N^B) = b < 0$. Similar to the steps taken in the main text, if $\sigma^A\xi^A > \sigma^B\xi^B$ then it follows

$$\begin{aligned}
\sigma^A\xi^A > \sigma^B\xi^B \quad &\Rightarrow \quad \frac{b}{Re(\lambda_N^A)}\xi_A > \frac{b}{Re(\lambda_N^B)}\xi_B \\
&\Rightarrow \quad \frac{\xi_A}{Re(\lambda_N^A)} < \frac{\xi_B}{Re(\lambda_N^B)}
\end{aligned}$$

and the syncreactivity measure for the transition $S \to A$ now becomes,

$$\tilde{\Xi} = 1 - \frac{\xi}{Re(\lambda_N)}. \tag{S59}$$

Similar to Ξ from Eq. (S58), $\tilde{\Xi}$ is a purely topological measure of the network topology. The network with higher $\tilde{\Xi}$ has larger $r(\boldsymbol{x}_s)$ and μ, i.e., if $\tilde{\Xi}^A > \tilde{\Xi}^B$, then $r^A(\boldsymbol{x}_s) \geq r^B(\boldsymbol{x}_s)$ and $\mu^A \geq \mu^B$.

Supplementary Note 15. EFFECTS OF SYNCREACTIVITY INDEX Ξ ON THE DYNAMICS

In this subsection, we compare the number of bubbling events and the amplitude of the bubbling events for the cases of two network topologies characterized by different syncreactivity Ξ. The same 10-node star and chain networks as in the main manuscripts are selected. Their Laplacian matrices are

$$L_c = \begin{bmatrix} 0 & 0 & 0 & \dots & 0 & 0 \\ 1 & -1 & 0 & \dots & 0 & 0 \\ 0 & 1 & -1 & \dots & 0 & 0 \\ \vdots & \vdots & \vdots & \ddots & \vdots & \vdots \\ 0 & 0 & 0 & \dots & -1 & 0 \\ 0 & 0 & 0 & \dots & 1 & -1 \end{bmatrix}, \tag{S60a}$$

$$L_s = \begin{bmatrix} 0 & 0 & 0 & \dots & 0 & 0 \\ 1 & -1 & 0 & \dots & 0 & 0 \\ 1 & 0 & -1 & \dots & 0 & 0 \\ \vdots & \vdots & \vdots & \ddots & \vdots & \vdots \\ 1 & 0 & 0 & \dots & -1 & 0 \\ 1 & 0 & 0 & \dots & 0 & -1 \end{bmatrix}. \tag{S60b}$$

We remark that the spectrum of the two Laplacian matrices above, corresponding to the chain and the star, is the same. The syncreactivity for the chain is $\Xi_c = 1.1536$ while the syncreactivity for the star is $\Xi_s = 0$. We use the same local dynamics and the coupling matrix as in (S28) and (S33) with the same constant coupling strength $\sigma = 4.4$. We set the variance of the added white noise to be 0.001. We simulate the coupled system 1000 times, each time for $1000s$. The integration of the stochastic ODE is done using Heun's method with a stepsize of $0.001s$. We keep track of the peaks in the norm of the motion transverse to the synchronization manifold as a function of time. If the value of a peak is larger than a given threshold, then we say that a bubbling event has occurred, and the peak norm of the transverse motion is recorded. Here, we set the threshold to be 0.5.

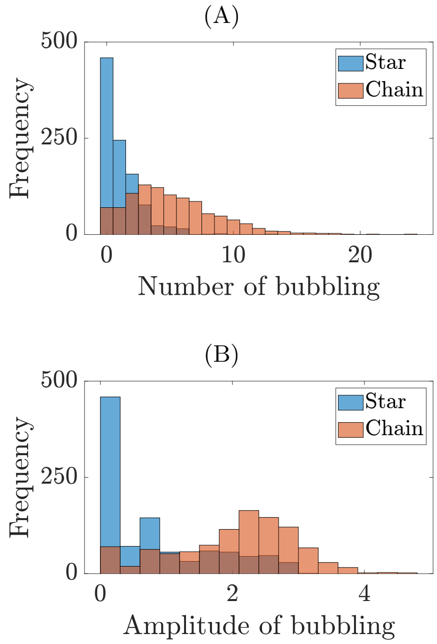

Supplementary Fig. 14. **Effect of the syncreactivity Ξ on the attractor bubbling.** Histograms of the number of bubbling events (A) and of the amplitudes of such events (B) recorded over 1000 different simulations. We use the same local dynamics and the coupling matrix as in Eqs. (S28) and (S33) with the same constant coupling strength $\sigma = 4.4$. We set the variance of the added white noise to be 0.001. The two 10-node network topologies are given by the Laplacian matrices in Eq. (S60). For the chain $\Xi_c = 1.1536$ and for the star, $\Xi_s = 0$.

Supplementary Fig. 14 shows the histogram for the number of bubbling events and amplitudes of such events in panels A and B, respectively. We note that bubbling events have occurred 5.11 and 1.11 times on average with medians of 5 and 1 during the $1000s$ interval for the chain and the star configurations, respectively. Also, the amplitudes of the bubbling events were 2.02 and 0.75 times on average with medians of 2.19 and 0.56 during the $1000s$ interval for the chain and the star configurations, respectively. We see that the systems coupled via the chain topology produce more bubbling events with higher amplitudes. These results indicate that in the presence of noise, a more reactive network topology is more susceptible to the occurrence of bubbling..

Supplementary Note 16. SYNCREACTIVITY Ξ FOR SYNTHETIC NETWORKS

In this section, we investigate syncreactivity Ξ from Eq. (S58) for randomly generated Erdos-Renyi networks (random networks) and scale-free networks.

For random networks, we set the number of nodes N and vary the connection probability p from 0.1 to 0.9. The connection probability determines if a directed unweighted link exists between any two nodes. We do not allow self-loops. For each pair of N and p, we keep generating random networks until we have 100 networks with a nonzero eigenvalue λ_2 of their Laplacian matrices. We then calculate the syncreactivity Ξ for these graphs.

Next, we use the static model from[28] to create scale-free graphs with N nodes. The method proposed by Goh *et al.* has the power-law exponent of the indegree distribution $\zeta_{in} = (1 + \eta_{in})/\eta_{in}$ and of the outdegree distribution $\zeta_{out} = (1 + \eta_{out})/\eta_{out}$ where $\eta_{in}, \eta_{out} \in (0,\ 1]$ are prescribed control parameters. First, two weights $p_i = i^{-\eta_{out}}$ and $q_i = i^{-\eta_{in}}$ are assigned to each node i for outgoing and incoming edges, respectively. Then, two different nodes i and j are selected randomly with normalized probabilities $p_i/\sum_k p_k$ and $q_j/\sum_k q_k$, respectively. An edge is created from i to j unless it already exists. This process is repeated until kN links are added where k is the average degree of the directed graph (i.e., the total number of edges divided by the number of nodes.) Here we set $k = 0.2N$ where 0.2 can be thought of as the density of the graph (number of edges divided by N^2.) We set $\eta_{in} = \eta_{out} = \eta$ and vary η between 0.5 and 1. For $\eta = 0.5$, the power law component is $\zeta_{in} = \zeta_{out} = 3$ (more heterogeneous network), and for $\eta = 1$, the power law component is $\zeta_{in} = \zeta_{out} = 2$ (more homogeneous network.) For each pair of N and η, we keep generating random graphs until we have 100 graphs with a directed spanning tree (i.e., for which the eigenvalue λ_2 of the Laplacian matrix is nonzero.)

Supplementary Fig. 15 shows the syncreactivity Ξ for Erdos-Renyi and scale-free networks in panels A and B, respectively. We see that for both cases, as the number of nodes N increases, the syncreactivity Ξ decreases. For Erdos-Renyi networks, as the connection probability p increases, Ξ decreases. For scale-free networks, as the network becomes more homogeneous ($\eta \to 1$), Ξ decreases. We thus conclude that the syncreactivity Ξ has an inverse relationship with the number of nodes, the connectivity probability of Erdos-Renyi networks, and the homogeneity of the degree distribution for scale-free networks.

Supplementary Note 17. SYNCREACTIVITY VS OTHER MEASURES OF SYNCHRONIZABILITY

Supplementary Fig. 16 shows the syncreactivity measure Ξ vs different measures of the synchronizability and non-normality. Overall we see the groups of selected networks represent a wide range in all the synchronizability measures and the non-normality.

Supplementary Note 18. REAL NETWORKS

In this section, we provide supplementary information about the real network topologies used in the main manuscript. The information is summarized in Table I. The source for the real network data is available at[29].

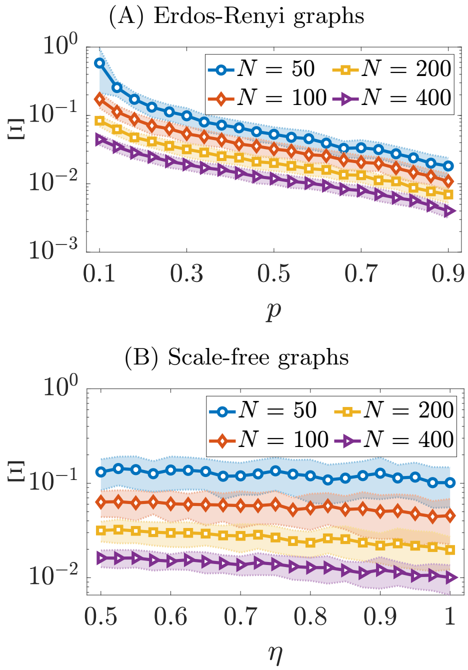

Supplementary Fig. 15. **The syncreactivity Ξ for directed unweighted Erdos-Renyi and directed unweighted scale-free graphs.** Plots show the mean value of Ξ as the number of nodes N, the connection probability p, and the scale-free parameter η varies. The shaded backgrounds denote the standard deviation. Each data point is averaged over 100 realizations.

Supplementary Note 19. REDUCTION OF THE SETTLING TIME VIA THE CWN STRATEGY

In this Section, we measure the settling time for achieving synchronization via the conventional constant coupling and the CWN strategy. We vary the parameters in the CWN strategy and plot the reduction obtained in comparison to the constant coupling strategy. We use the same local dynamics and coupling function (Lorenz) as in Eq. (S9). We use the unweighted directed chain network topology with 10 nodes. The Laplacian matrix for this network is given by Eq. (S60a).

We set the initial conditions to be close to the synchronous solution such that the norm of the transverse perturbation at the initial time is 10^{-5}. We define the settling time T_s as the time it takes for the norm of the transverse perturbations to reach zero, averaged over several choices of the initial conditions. In practice, we measure T_s as the time it takes for the norm of the transverse perturbations to reach 10^{-10}. This threshold is chosen such that it is above our tolerance settings of 10^{-13} for the ode integration function `ode113` in MATLAB 2024a.

We define

$$\%\ \text{normalized}\ T_s = \frac{T_s^{CWN}}{T_s^{constant}} 100 \qquad \text{(S61)}$$

where $T_s^{constant}$ is the settling time when the constant coupling strategy is implemented, i.e., $\sigma = \bar{\sigma}$, and T_s^{CWN} is the settling time when $\sigma = \sigma(t)$ via the CWN in Eq. (S17). Supplementary Fig. 17 shows that the settling time will decrease for all values of the parameters β and $\gamma \neq 1$ when the CWN strategy is implemented. Remind that $\gamma = 1$ corresponds to the case of constant coupling strategy, i.e., $\sigma = \bar{\sigma}$. The lowest % normalized T_s achieved for $\bar{\sigma}$ equal to 4, 8, and 12 are 8%, 29%, and 51%, respectively. We see a greater reduction in the settling time via the CWN strategy for lower $\bar{\sigma}$, which is close to the threshold for synchronization with constant coupling $\sigma^* = 2.5$.

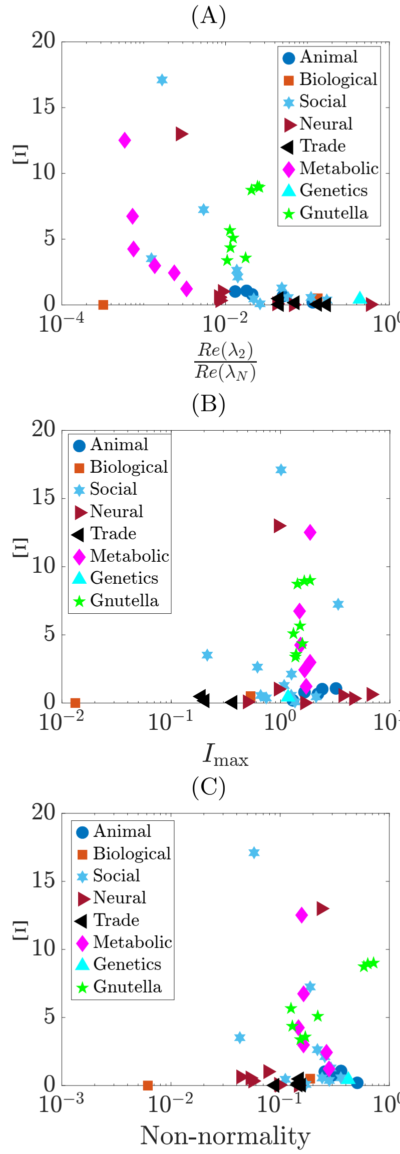

Supplementary Fig. 16. **The syncreactivity Ξ of real networks.** The syncreactivity Ξ vs (A) the real part eigenratio $Re(\lambda_2)/Re(\lambda_N)$, (B) the maximum imaginary part among all the eigenvalues $I_{\max}$ of the Laplacian, and (C) the non-normality $\|L^\top L - LL^\top\|_2/\|L\|_2^2$ for a collection of real networks of different categories.

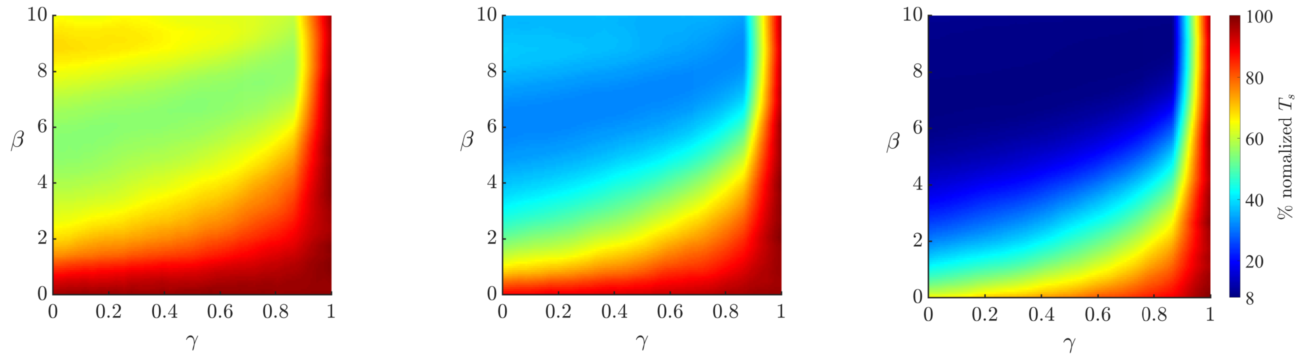

Supplementary Fig. 17. **The % normalized T_s for three values of the average coupling strength $\bar{\sigma}$ as the parameters γ and β for the CWN strategy are varied.** Panels A, B, and C correspond to $\bar{\sigma}$ equal to 12, 8, and 8, respectively. The threshold for synchronization using a constant coupling for this setup is $\sigma = 2.5$.

Supplementary Note 20. REACTIVITY IN NETWORKS OF PHASE OSCILLATORS

In this section, we analyze the reactivity of networks composed of N homogenous Kuramoto phase oscillators. The dynamic of the i-th oscillator can be described as:

$$\dot{x}_i = \omega + \sigma \sum_j A_{ij} \sin(x_j - x_i) \tag{S62}$$

where ω is the natural frequency of the isolated node, A is the connectivity matrix ((the network adjacency matrix)), and $\sigma \geq 0$ is the coupling strength.

This network admits the global synchronous solution $s(t) = x_1(t) = \cdots = x_N(t)$[30], which is governed by the differential equation

$$\dot{s}(t) = \omega \tag{S63}$$

By following the steps defined in the main text and in Supplementary Note 1, we first linearize the network equations about the synchronous solution s(t) thus obtaining the variational equations:

$$\begin{aligned} \delta\dot{x}_i &= \sigma \sum_j A_{ij}(\delta x_j - \delta x_i) = \\ &= \sigma \sum_j L_{ij} \delta x_j \quad i = 1, \ldots, N \end{aligned} \tag{S64}$$

where L is the Laplacian matrix corresponding to the connectivity matrix A, i.e., $L_{ij} = A_{ij} - \delta_{ij} \sum_j A_{ij}$, i,j=1,...,N. We can then remove the parallel mode corresponding to the synchronous solution from the N equations and study the reactivity of the system:

$$\delta\dot{\boldsymbol{x}}_\perp = \sigma L_\perp \delta\boldsymbol{x}_\perp, \tag{S65}$$

where the matrix $L_\perp$ is defined as in the main text. Notice that the network topology affects the reactivity (as discussed in the main text for the general case) but not the synchronous solution $s(t)$ (see Eq. (S63). Moreover, in this case, the reactivity is independent of the particular state along the synchronous attractor $s(t)$ about which one is linearizing. Here the sign of reactivity is the same as that of the algebraic connectivity: $r = \sigma \times 2e_1(L_\perp + L_\perp^\top) = \sigma\xi$. Hence, the reactivity r is positive (negative) for networks with positive (negative) algebraic connectivity ξ. For example, Supplementary Fig. 18 shows the network algebraic connectivity ξ for the chain topology (red dots) and the star topology (blue dots) with N nodes, $N = 3, 4, \ldots, 15$. The Laplacian matrices L_c and L_s for the chain and the star topologies, respectively, are given in Eq. (S60). We see for $N \geq 6$ nodes, the chain topology has positive ξ (and thus positive reactivity r) while the star topology has a negative ξ (and thus a negative reactivity r.)

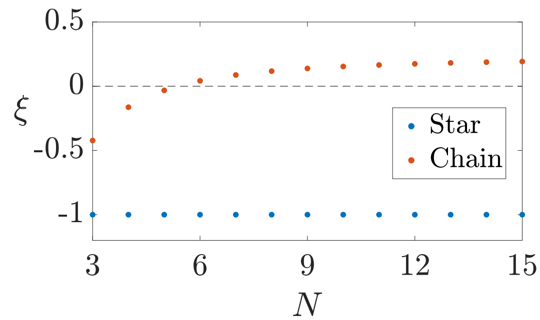

Supplementary Fig. 18. Network algebraic connectivity ξ of the chain (red dots) and the star (blue dots) networks with N nodes. Both star and chain topologies are directed and unweighted.

Here we do not cover the case of the heterogeneous network of Kuramoto oscillators. This case is the subject of ongoing work and will be presented in a forthcoming publication.

REFERENCES

[1] Stewart, G. W. A krylov–schur algorithm for large eigenproblems. *SIAM Journal on Matrix Analysis and Applications* **23**, 601–614 (2002).

[2] Saad, Y. *Numerical Methods for Large Eigenvalue Problems* (Society for Industrial and Applied Mathematics, 2011).

[3] Delattre, B., Barthélemy, Q., Araujo, A. & Allauzen, A. Efficient bound of Lipschitz constant for convolutional layers by Gram iteration. In Krause, A. *et al.* (eds.) *Proceedings of the 40th International Conference on Machine Learning*, vol. 202 of *Proceedings of Machine Learning Research*, 7513–7532 (PMLR, 2023).

[4] Mises, R. & Pollaczek-Geiringer, H. Praktische verfahren der gleichungsauflösung. *ZAMM-Journal of Applied Mathematics and Mechanics/Zeitschrift für Angewandte Mathematik und Mechanik* **9**, 58–77 (1929).

[5] Nazerian, A., Phillips, D., Frasca, M. & Sorrentino, F. The reactability of discrete time systems. *IEEE Control Systems Letters* **7**, 3657–3662 (2023).

[6] Ott, E. *Chaos in dynamical systems* (Cambridge university press, 2002).

[7] Huang, L., Chen, Q., Lai, Y.-C. & Pecora, L. M. Generic behavior of master-stability functions in coupled nonlinear dynamical systems. *Phys. Rev. E* **80**, 036204 (2009).

[8] Nazerian, A., Phillips, D., Makse, H. A. & Sorrentino, F. Single-integrator consensus dynamics over minimally reactive networks. *IEEE Control Systems Letters* **7**, 2437–2442 (2023).

[9] Belykh, I. V., Belykh, V. N. & Hasler, M. Blinking model and synchronization in small-world networks with a time-varying coupling. *Physica D: Nonlinear Phenomena* **195**, 188–206 (2004).

[10] So, P., Cotton, B. C. & Barreto, E. Synchronization in interacting populations of heterogeneous oscillators with time-varying coupling. *Chaos: An Interdisciplinary Journal of Nonlinear Science* **18** (2008).

[11] Chen, L., Qiu, C. & Huang, H. Synchronization with on-off coupling: Role of time scales in network dynamics. *Physical Review E* **79**, 045101 (2009).

[12] Buscarino, A., Frasca, M., Branciforte, M., Fortuna, L. & Sprott, J. C. Synchronization of two rössler systems with switching coupling. *Nonlinear Dynamics* **88**, 673–683 (2017).

[13] Parastesh, F. *et al.* Synchronizability of two neurons with switching in the coupling. *Applied Mathematics and Computation* **350**, 217–223 (2019).

[14] Li, S., Sun, N., Chen, L. & Wang, X. Network synchronization with periodic coupling. *Phys. Rev. E* **98**, 012304 (2018). URL `https://link.aps.org/doi/10.1103/PhysRevE.98.012304`.

[15] Olfati-Saber, R. & Murray, R. Consensus problems in networks of agents with switching topology and time-delays. *IEEE Transactions on Automatic Control* **49**, 1520–1533 (2004).

[16] Ashwin, P., Buescu, J. & Stewart, I. Bubbling of attractors and synchronisation of chaotic oscillators. *Physics Letters A* **193**, 126–139 (1994).

[17] de S. Cavalcante, H. L. D., Oriá, M., Sornette, D., Ott, E. & Gauthier, D. J. Predictability and suppression of extreme events in a chaotic system. *Phys. Rev. Lett.* **111**, 198701 (2013).

[18] Van den Broeck, C., Parrondo, J. M. R., Toral, R. & Kawai, R. Nonequilibrium phase transitions induced by multiplicative noise. *Phys. Rev. E* **55**, 4084–4094 (1997).

[19] Nguyen, L. H. & Hong, K.-S. Synchronization of coupled chaotic fitzhugh–nagumo neurons via lyapunov functions. *Mathematics and Computers in Simulation* **82**, 590–603 (2011).

[20] Larger, L. & Dudley, J. M. Optoelectronic chaos. *Nature* **465**, 41–42 (2010).

[21] Murphy, T. E. *et al.* Complex dynamics and synchronization of delayed-feedback nonlinear oscillators. *Phil. Trans. R. Soc. A* **368**, 343–366 (2010).

[22] Ravoori, B. *et al.* Adaptive synchronization of coupled chaotic oscillators. *Phys. Rev. E* **80**, 056205 (2009).

[23] Ravoori, B. *et al.* Robustness of optimal synchronization in real networks. *Physical review letters* **107**, 034102 (2011).

[24] Hart, J. D., Roy, R., Müller-Bender, D., Otto, A. & Radons, G. Laminar chaos in experiments: Nonlinear systems with time-varying delays and noise. *Phys. Rev. Lett.* **123**, 154101 (2019).

[25] Banerjee, A., Hart, J. D., Roy, R. & Ott, E. Machine learning link inference of noisy delay-coupled networks with optoelectronic experimental tests. *Phys. Rev. X* **11**, 031014 (2021).

[26] Farmer, J. D. Chaotic attractors of an infinite-dimensional dynamical system. *Physica D* **4**, 366–393 (1982).

[27] Le Berre, M. *et al.* Conjecture on the dimensions of chaotic attractors of delayed-feedback dynamical systems. *Physical Review A* **35**, 4020 (1987).

[28] Goh, K.-I., Kahng, B. & Kim, D. Universal behavior of load distribution in scale-free networks. *Phys. Rev. Lett.* **87**, 278701 (2001). URL `https://link.aps.org/doi/10.1103/PhysRevLett.87.278701`.

[29] Kunegis, J. KONECT – The Koblenz Network Collection. In *Proc. Int. Conf. on World Wide Web Companion*, 1343–1350 (2013). URL `http://dl.acm.org/citation.cfm?id=2488173`.

[30] Strogatz, S. H. From kuramoto to crawford: exploring the onset of synchronization in populations of coupled oscillators. *Physica D: Nonlinear Phenomena* **143**, 1–20 (2000).

TABLE I. **Real Networks**. Detailed description of the real networks considered in the main manuscript. Here, LSCC is short for the largest strongly connected component.

Type	Name	Size	LSCC size	Node Info	Edge Info
Animal[29]	Japanese macaques	62	38	Animal, macaque	Dominance: only those aggressive interactions were analyzed that led to an outcome in which the lost and the winner could be categorized unambiguously
	Cattle	28	20	Animal, cattle	
	Sheep	28	22	Animal, sheep	
	Bison	26	26	Animal, bison	
	Hens	32	31	Animal, hens	
Biological[29]	human-protein-interactions (Figeys)	2239	8	Human, proteins	Protein Interactions.
	human-protein-interactions (Stelzl)	1706	1493	Human, proteins	
Social[29]	social-adolescenthealth-interactions	2539	2155	Human, social	Interactions: social relationships and communication patterns within different social contexts.
	social-filmtrust-trust	874	267	Human, user	
	social-physicians-trust	241	95	Human, physician	
	social-residencehall-friendship	217	214	Human, person	
	social-seventhgraders-proximity	29	29	Human, student	
	social-highschool-friendship	70	67	Human, boy	
Gnutella[29]	Gnutella (08)	6301	2068	Computer, Host	Connections between the computers.
	Gnutella (09)	8114	2624		
	Gnutella (04)	10876	4317		
	Gnutella (05)	8846	3234		
	Gnutella (06)	8717	3226		
	Gnutella (24)	26518	6352		
	Gnutella (25)	22687	5153		
	Gnutella (30)	36682	8490		
Metabolic	net CE	1222	1079	metabolites	the proteins/enzymes interaction
	net CQ	436	324		
	net CT	493	384		
	net MJ	1089	1003		
	net SC	1559	1414		
Neural	cat brain	65	65	neurons, neuronal populations, or regions	functional connectivity
	rat brain 1	503	502		
	mouse brain	213	213		
	rat brain 2	503	502		
	rat brain 3	496	493		
	rhesus brain 1	242	242		
	rhesus brain 2	91	11		
Trade	net trade basic	24	22	Country	Trade relationship between any two countries
	net trade minerals	24	24		
	net trade crude	24	24		
	net trade food	24	24		
	net trade crude	24	21		
Genetics	Human (cancer)	4049	9	Genes and regulators	The physical and/or regulatory relationships.